Dynamic behavior analysis of cracked rotor

Oh Sung Jun[a], Mohamed S. Gadala[b],*

[a]*Department of Mechanical Engineering, Jeonju University, Jeonju 560-759, Republic of Korea*
[b]*Department of Mechanical Engineering, University of British Columbia, Vancouver, BC, Canada V6T 1Z4*

Abstract

In the present study, the additional slope is used to consider the crack breathing, and is expressed explicitly in the equation of motion as one of the inputs to produce the bending moment at the crack position. Inversely, the additional slope is calculated by integrating on the crack region based on a fracture mechanics concept. The response of a cracked rotor is formulated based on the transfer matrix method. The transient behavior due to the crack breathing is considered by introducing a 'moving' Fourier-series expansion concept to the additional slope. The time-varying harmonic components of the additional slope are used to calculate the harmonic responses. The application considered is a general rotor model composed of multiple shafts, disks and cracks, and resilient bearings at both ends. Verification analysis is carried out for a simple rotor model similar to those found in the literature. Using the additional slope, the cracked rotor behavior is explained by the crack depth and rotation speed increase. It is shown that region on the crack front line having the dominant stress intensity factor value moves from the central area to both ends, as the crack depth increases. The result matches well with the crack propagation pattern shown in a bench mark test in the literature. Whirl orbits near the critical and sub-critical speed ranges of the rotor are discussed. It is shown that there exists some speed range near the critical speed, where the temporary whirl direction reversal and phase shift exist. When an unbalance is applied, the peculiar features, such as the whirl direction reversal and phase shift, disappear.
© 2007 Elsevier Ltd. All rights reserved.

1. Introduction

Transverse cracks in horizontal rotating shafts experience repeated opening and closing due to gravity force. The repeated opening and closing induce large fatigue stresses on the crack front that normally leads to crack propagation. This may severely damage the rotating machinery and lead to catastrophic and dangerous failure. This has led to great effort in developing on-line fault detection systems and reliable methods of diagnostics and analysis of such problems in recent years.

Since a crack directly affects the stiffness, the continuous change of the crack open status renders the system stiffness characteristics to be nonlinear. Dimarogonas and Paipetis [1] and Dimarogonas and

*Corresponding author. Tel.: +1 604 822 2777; fax: +1 604 822 2403.
E-mail addresses: junos@jeonju.ac.kr (O.S. Jun), gadala@mech.ubc.ca (M.S. Gadala).

Papadopoulos [2] calculated a local compliance based on the fracture mechanics, and the local compliance was used by many researches [3,4]. The local compliances on the crack direction with fully open crack and on the crack edge direction with half-open crack were used in calculating the response by analyzing the applied forces and by vectorially adding the corresponding deflections during the rotation of shaft [2].

Several people since the 1970s [5–8] have considered the stiffness change due to a crack and incorporated this into the equations of motion, in the form of a time-periodic function changing between the maximum stiffness value for the fully closed crack status and a minimum value for the fully open crack status. Jun et al. [9] expressed the equation of motion with the response-dependent stiffness in a simple rotor. Using the crack model [1] based on the fracture mechanics [10] and the idea of cross-coupled stiffness, Jun et al. [9] explained the crack breathing and the dynamic behavior of cracked rotor through the numerical integration (Runge–Kutta method). The crack openness was determined through the response solved by the governing equation, and the response-dependent stiffness was calculated by integrating over only the open crack area. Several successive researches using the same method were published [11,12]. However, because of the difficulty in modeling, the research models were limited to a simple rotor system composed of mass, damping and spring components.

In studying more realistic rotor models, the finite element method has been used by many researchers. Nelson and Nataraj [13] considered the rotating stiffness variation in the model and solved the response by the perturbation method. Keiner and Gadala [14] modeled cracked region using 3D solid element and compared the responses using the suggested linearized 3D finite element model and the transient 3D finite element model.

The transfer matrix method has also been used for rotor dynamics in many researches. Most commonly used transfer matrix method was based on the lumped-mass model [15,16]. The transfer matrix for the shaft element with distributed mass and stiffness, based on the Euler beam theory, was used in practical rotor system [17]. When the lumped mass shaft model is used, there must be a sufficient number of stations to represent the higher modes of interest. Tsai and Wang [18] used the transfer matrix based on the Timoshenko beam theory in order to formulate the free bending vibration of the stationary shaft having a transverse open crack and to derive a diagnostic method. They also expanded the transfer matrix for free vibration analysis for the rotor having multiple steps, multiple open cracks, multiple disks and simply supported boundary condition at both ends [19].

From the complex governing equation for a rotating shaft having the gyroscopic effect and torque, Jun [20] derived the complex transfer matrix in a closed form for the distributed parameter model based on the Timoshenko beam theory, and used it for deriving the influence coefficient for a general rotor model having the resilient bearings at both ends. Using the idea, the response at an arbitrary position has been analytically expressed.

The final purpose of the research on the cracked rotor is to extract a proper diagnostic method. For this purpose, a more precise simulation of the cracked rotor behavior is required. This paper is mainly focused on the derivation of a proper method for simulation of the cracked rotor dynamic motion with a deeper consideration of the physical phenomena associated with the cracks and the general rotor model. In the present paper, the linear transfer function of the rotor system is used, and the additional slope at crack position as a self-excitation source is explicitly expressed and incorporated in the equation. By considering the coupling between the response and the additional slope due to crack breathing, an iterative method is proposed to simulate the dynamic behavior of cracked rotor. The response at the crack location is analytically expressed using the method of Ref. [20]. The additional slope at the crack during revolution is expressed in terms of the bending moment, which is one of the responses, and is calculated by integrating over only the open crack area. The developed approach is used to model a general rotor with multiple disks, shafts and cracks, and resilient bearings at each end. Another simpler model is used for the sake of comparing results with those available in the literature and for testing the developed approach. Changes in the introduced additional slope with the crack depth and rotation speed are discussed. The distribution of the maximum stress intensity factor (SIF) with crack propagation is also discussed. Peculiar orbit characteristics are discussed near the critical and sub-critical speed ranges.

2. Behavior of cracked rotor

2.1. Motion coupled with crack opening

The key issues in developing an accurate modeling technique for a cracked rotor are the reduced stiffness of the cracked cross-section, the variation of stiffness over one revolution due to the opening and closing of the crack (crack breathing) and the complexity in geometry of the rotor, in particular in the region of the developing crack. The crack opening reduces the local stiffness, and also makes the stiffness change continuously. The crack breathing mechanism has been modeled in a variety of ways, all resulting in a time-varying local compliance matrix, which is incorporated into the dynamic equations for the rotor. The equations of motion have been solved analytically, in a linearized form, or numerically through time-integration. Full understanding of the shaft motion includes studying the change of slope, bending moment and shear force distributions as well as the deflection of the shaft; the first three items are directly related to the last one.

The crack opening is mainly dependent on the gravity, if there is no other forcing element, and it occurs due to the bending moment resulting from gravity loads. The bending moment may be considered, however, as one of the responses of the shaft under the motion and the problem is, therefore, strongly coupled each other. Fig. 1 shows a diagrammatic sketch expressing the coupled phenomenon happening during a revolution.

The partially hatched circles in Fig. 1 show a spinning shaft at small angle intervals. At the angle $(\Omega t)_1$, according to the bending moment around crack, the crack opening status is determined. The magnitude and direction of bending moment determine the crack opening status, which can be expressed as the additional slope $\Delta\alpha$ at crack. At the next angle $(\Omega t)_2$, even though the shaft revolution is actually continuous, the response including the bending moment is determined and another additional slope $\Delta\alpha$ is calculated.

2.2. Coordinates system and variable definitions

Figs. 2 and 3 show the state variables in $X-Z$ (vertical) and $X-Y$ (horizontal) planes on ith shaft element of the normal rotor, respectively. Introducing the complex quantities yields the complex state variables as follows:

$$\begin{aligned}
U_i &= Y_i + jZ_i, \\
\alpha_i &= \phi_i + j\theta_i, \\
M_i &= M_{z,i} + jM_{y,i}, \\
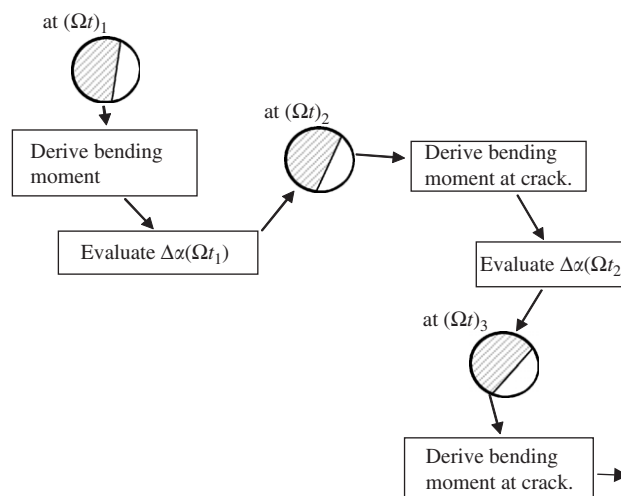V_i &= V_{y,i} + jV_{z,i},
\end{aligned} \tag{1}$$
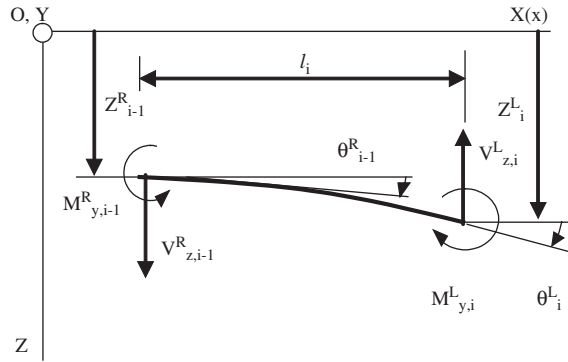

Fig. 1. Coupling of crack opening and response.

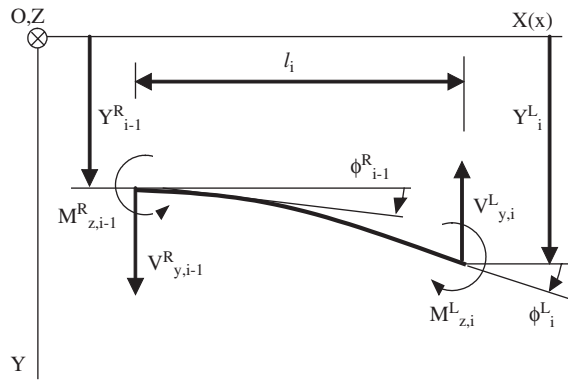Fig. 2. State variables of ith shaft element in X–Z plane.

Fig. 3. State variables of ith shaft element in X–Y plane.

where Z_i, θ_i, $M_{y,i}$ and $V_{z,i}$ are the displacement, slope, bending moment and shear force in X–Z plane, respectively, as shown in Fig. 2 and Y_i, ϕ_i, $M_{z,i}$ and $V_{y,i}$ are the displacement, slope, bending moment and shear force in X–Y plane, respectively, as shown in Fig. 3. The subscript i is the node number, and the superscripts R and L denote the right- and left-hand sides of nodes, respectively.

The slope α, moment M and shear force V for the Timoshenko beam model has the following relations [21]:

$$
\begin{aligned}
\alpha &= \frac{\mathrm{d}U}{\mathrm{d}x}, \\
M &= EI\frac{\mathrm{d}^2 U}{\mathrm{d}x^2} - jT\frac{\mathrm{d}U}{\mathrm{d}x}, \\
V &= EI\frac{\mathrm{d}^3 U}{\mathrm{d}x^3} - jT\frac{\mathrm{d}^2 U}{\mathrm{d}x^2} + \rho A r_0^2(\omega^2 - 2\omega\Omega)\frac{\mathrm{d}U}{\mathrm{d}x},
\end{aligned}
\tag{2}
$$

where E and ρ are Young's modulus and mass density, respectively, and T is the torque on each end of the shaft. A and I are the area and area moment of inertia of the cross-section, r_0 is the radius of gyration, Ω is the rotating speed and ω is the natural frequency.

The transfer matrix for dynamic analysis, derived from rotating Timoshenko beam theory, and the transfer matrix for static analysis, are introduced in Appendix A [20] and Appendix B, respectively.

3. Allocation of crack in modeling

3.1. Consideration of crack opening status

Crack opening status may be determined from the bending moments at both ends of the shaft having a crack at its mid-span. From the bending moments M_ξ and M_η on a rotating (ξ, η) coordinate frame, as shown in Fig. 4, the signs of the total SIF $K^I = K^I_\xi + K^I_\eta$ (superscript I, denoting the usual crack opening mode I in the fracture mechanics) along the crack tip line are determined. The additional slope is obtained by integrating on the crack region excluding the region of negative K^I since the compression state of stress indicates that the crack is closed and not contributing to the additional deflection [9,22].

As shown in Fig. 5, the SIF $K^I_{M_\eta}$, due to a positive value of bending moment M_η, on the crack front of a strip having thickness dw is equal to the value for the crack under pure bending. The SIF $K^I_{M_\eta}$ is given by [10]

$$K^I_{M_\eta}(w) = \sigma_1(w)\sqrt{\pi\alpha}F(\alpha/\alpha'),\tag{3}$$

Fig. 4. Moments applied on a shaft containing a transverse crack.

Fig. 5. Cross-section of shaft at crack position.

where $\sigma_1(w) = (-M_\eta)\,(\alpha'/2)/\pi D^4/64$,

$$F(\alpha/\alpha') = \sqrt{\frac{2\alpha'}{\pi\alpha}\tan\frac{\pi\alpha}{2\alpha'}}\,\frac{0.923 + 0.199\big(1 - \sin\,\pi\alpha/2\alpha'\big)^4}{\cos\,\pi\alpha/2\alpha'}$$

and $\alpha' = \sqrt{D^2 - 4w^2}$.

α' and α are the total width and crack depth of the strip having thickness dw, respectively, and D is the diameter of shaft. w is the position of the strip from ξ axis along the positive η direction.

For the moment M_ξ on the same strip, the SIF $K^I_{M_\xi}$ is expressed in a similar manner as follows:

$$K^I_{M_\xi}(w) = \sigma_2(w)\sqrt{\pi\alpha}F'(\alpha/\alpha'), \tag{4}$$

where $\sigma_2(w) = (-M_\xi)w/(\pi D^4/64)$,

$$F'(\alpha/\alpha') = \sqrt{\frac{2\alpha'}{\pi\alpha}\tan\frac{\pi\alpha}{2\alpha'}}\,\frac{0.752 + 2.02(\alpha/\alpha') + 0.37\big(1 - \sin\,\pi\alpha/2\alpha'\big)^3}{\cos\,\pi\alpha/2\alpha'}.$$

The total SIF $K^I(w)$ is given by

$$K^I(w) = K^I_{M_\eta}(w) + K^I_{M_\xi}(w). \tag{5}$$

Castigliano's theorem gives the additional slopes due to the crack for η and ξ axes, respectively, as

$$\Delta\alpha_{\eta,\text{crack}} = \frac{1}{2E}\int_A (K^I_{M_\eta} + K^I_{M_\xi})\frac{\partial K^I_{M_\eta}}{\partial M_\eta}\,\mathrm{d}A, \tag{6}$$

$$\Delta\alpha_{\xi,\text{crack}} = \frac{1}{2E}\int_A (K^I_{M_\eta} + K^I_{M_\xi})\frac{\partial K^I_{M_\xi}}{\partial M_\xi}\,\mathrm{d}A, \tag{7}$$

where

$$\frac{\partial K^I_{M_\eta}}{\partial M_\eta} = \frac{\alpha'/2}{\pi D^4/64}\sqrt{\pi\alpha}F(\alpha/\alpha'),$$

$$\frac{\partial K^I_{M_\xi}}{\partial M_\xi} = \frac{w}{\pi D^4/64}\sqrt{\pi\alpha}F'(\alpha/\alpha').$$

Assuming a completely open crack, the area integration may be explicitly performed by

$$\int_A f\,\mathrm{d}A = \int_{-\sqrt{a(D-a)}}^{\sqrt{a(D-a)}}\int_0^{a-(D/2-\sqrt{(D/2)^2-w^2})} f\,\mathrm{d}\alpha\,\mathrm{d}w. \tag{8}$$

3.2. Locating a crack at node

Consider an element between nodes i and $i+1$. The relation between the state vectors at both ends of the shaft element is as follows:

$$\begin{pmatrix} U_{i+1} \\ \alpha_{i+1} \\ M_{i+1} \\ V_{i+1} \end{pmatrix}^L = [C]_i \begin{pmatrix} U_i \\ \alpha_i \\ M_i \\ V_i \end{pmatrix}^R,$$

where $[C]_i$ is the transfer matrix of the ith shaft element having a crack at its mid-span. The superscripts L and R denote the left- and right-hand sides of the corresponding nodes, respectively. The additional slope due to a crack opening under bending moment at both ends of the cracked shaft can be expressed as shown in the above section.

The model in this study is, however, a little different from the crack model of Ref. [10], because the bending moments at each end of a shaft element are different from each other. Nevertheless, if we locate the crack at a node, this ambiguity may be alleviated. If a crack is located at the ith node, the change in the response may be expressed by simply adding an extra slope due to crack opening to the point transfer matrix, i.e.,

$$\begin{Bmatrix} U_i \\ \alpha_i \\ M_i \\ V_i \end{Bmatrix}^R = \begin{bmatrix} 1 & 0 & 0 & 0 \\ 0 & 1 & 0 & 0 \\ 0 & 0 & 1 & 0 \\ 0 & 0 & 0 & 1 \end{bmatrix} \begin{Bmatrix} U_i \\ \alpha_i \\ M_i \\ V_i \end{Bmatrix}^L + \begin{Bmatrix} 0 \\ \Delta\alpha \\ 0 \\ 0 \end{Bmatrix}. \tag{9}$$

The bending moments at both sides of the node, which determines the additional slope, are of the same magnitude. Other variables except the slope, i.e., the deflection and the shear force, have same values at both sides of the node.

Expressing the state vectors at a node with a crack using the notations in Appendix A, the relation is written as follows:

$$\{s\}_i^R = \{s\}_i^L + \{c\}_i, \tag{10}$$

where

$$\{s\}_i = \begin{Bmatrix} U_i \\ \alpha_i \\ M_i \\ V_i \end{Bmatrix} \quad \text{and} \quad \{c\}_i = \begin{Bmatrix} 0 \\ \Delta\alpha \\ 0 \\ 0 \end{Bmatrix}.$$

4. Response of a cracked rotor

The elastodynamic behavior of a thick uniform shaft is described by considering the rotary inertia and shear deformation of the cross-section. Especially for a rotating shaft, the gyroscopic effect due to the rotation is also considered. Introducing the complex displacement

$$u(x, t) = y(x, t) + jz(x, t), \tag{11}$$

the equation of motion of a rotating horizontal shaft under the gravity effect is written as follows:

$$EI\frac{\partial^4 u}{\partial x^4} - jT\frac{\partial^3 u}{\partial x^3} - \left(\frac{EI\rho}{\kappa G} + \rho A r_0^2\right)\frac{\partial^4 u}{\partial x^2 \partial t^2} + j2\Omega\rho A r_0^2\frac{\partial^3 u}{\partial x^2 \partial t} + j\frac{T\rho}{\kappa G}\frac{\partial^3 u}{\partial x \partial t^2}$$

$$+ \rho A r_0^2\frac{\rho}{\kappa G}\frac{\partial^4 u}{\partial t^4} - j2\Omega\rho A r_0^2\frac{\rho}{\kappa G}\frac{\partial^3 u}{\partial t^3} + \rho A\frac{\partial^2 u}{\partial t^2} = j\rho A g, \tag{12}$$

where G is the shear modulus, κ the inverse of the generally used form factor, and g the gravitational acceleration. To simulate the response of a rotor having a crack (or cracks) it is necessary to consider the gravity response as well as the unbalance response because the crack breathing is fundamentally depending on gravity. The steady-state solution of the above equation is a time-independent one, i.e., is a static solution, as follows:

$$u(x, t) = jz_g(x). \tag{13}$$

If we consider the response due to the unbalance and the crack, the steady-state response is expressed as follows:

$$u(x, t) = u_u(x, t) + u_c(x, t). \tag{14}$$

If a rotating system does not have a crack, the response due to unbalance excitation and gravity effect may be expressed graphically as shown in Fig. 6. If the rotating system has a crack, the shaft motion has a different form. At first, the gravity response is no longer expressed as a z component only. For example, if we consider the
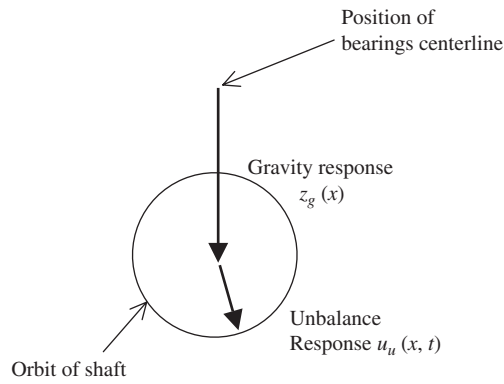
Fig. 6. Orbit of rotating shaft when having no crack.
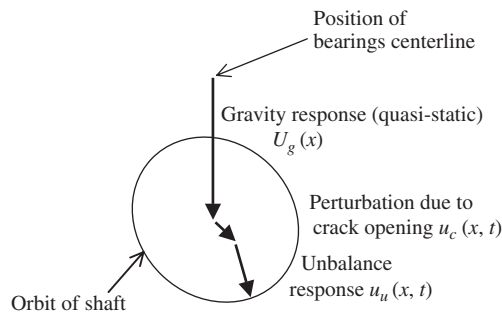

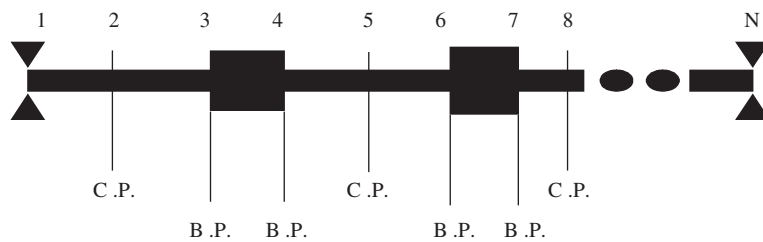Fig. 7. Orbit of rotating shaft when having a crack.

Fig. 8. General rotor model.

shaft at a given instant of time with a partially opened crack state, the center of the shaft would be shifted slightly in the y direction. Thus, a quasi-static gravity response is considered. Next, the response of the shaft having a crack includes the response component $u_c(x,t)$, which is considered as a perturbed term in this study as shown in Fig. 7. Crack breathing induces the perturbed term in the response. In Fig. 7, the difference between the upper case U in $U(x)$ and the lower-case u in $u(x,t)$ is the time dependency.

4.1. Crack and unbalance induced dynamic response

The influence coefficient, which can easily be used in calculating the solution for dynamic excitation such as unbalance, has been introduced in a previous study [20]. The state vector and the transfer matrix for the dynamic analysis are given in Appendix A.

Fig. 8 shows a general rotor having N nodes with two resilient bearings at both ends. B.P and C.P. indicate the planes having the unbalance mass and crack, respectively. For the unbalance masses on nodes Bi and the cracks on nodes Ci, the equation of the entire system is written as follows:

$$\{s\}_N^L = \prod_{i=1}^{N-1}[F]_i\{s\}_1^R + \prod_{i=B1}^{N-1}[F]_i\{u\}_{B1} + \prod_{i=B2}^{N-1}[F]_i\{u\}_{B2} + \cdots + \prod_{i=Bi}^{N-1}[F]_i\{u\}_{Bi}$$
$$+ \cdots + \prod_{i=C1}^{N-1}[F]_i\{c\}_{C1} + \prod_{i=C2}^{N-1}[F]_i\{c\}_{c2} + \cdots + \prod_{i=Ci}^{N-1}[F]_i\{c\}_{Ci} + \cdots, \tag{15}$$

or

$$\{s\}_N^L = T\{s\}_1^R + Q^{B1\sim N}\{u\}_{B1} + Q^{B2\sim N}\{u\}_{B2} + \cdots + Q^{Bi\sim N}\{u\}_{Bi} + \cdots$$
$$+ Q^{C1\sim N}\{c\}_{C1} + Q^{C2\sim N}\{c\}_{C2} + \cdots + Q^{Ci\sim N}\{c\}_{Ci} + \cdots, \tag{16}$$

where $[F]_i$ is the transfer matrix for ith shaft element, $Q^{r\sim s}$ the multiplication of transfer matrixes between nodes r and s, T the total transfer matrix between nodes 1 and N, and the vectors are expressed as

$$\{s\}_N^L = \begin{Bmatrix} U_N \\ \alpha_N \\ 0 \\ k_N U_N \end{Bmatrix}, \quad \{s\}_1^R = \begin{Bmatrix} U_1 \\ \alpha_1 \\ 0 \\ -k_1 U_1 \end{Bmatrix}, \quad \{u\}_{Bi} = \begin{Bmatrix} 0 \\ 0 \\ 0 \\ m_i e_i \Omega^2 \mathrm{e}^{j(\Omega t + \beta_i)} \end{Bmatrix} \quad \text{and} \quad \{c\}_{Ci} = \begin{Bmatrix} 0 \\ \Delta\alpha_{Ci}(t) \\ 0 \\ 0 \end{Bmatrix}$$

and where k_1 and k_N are the stiffness for the resilient bearings at nodes 1 and N, respectively, and $m_i e_i$ and β_i are, respectively, the magnitude and orientation of the unbalance at node i.

Considering the boundary conditions for the resilient bearings at nodes 1 and N, respectively, and solving for U_1^R and α_1^R, we obtain

$$U_1^R = \sum_{No.(Bi)} \frac{\begin{vmatrix} -(q_{14}^{Bi\sim N}k_N - q_{44}^{Bi\sim N}) & (t_{12}k_N - t_{42}) \\ -q_{34}^{Bi\sim N} & t_{32} \end{vmatrix}}{\begin{vmatrix} (t_{11}k_N - t_{14}k_1k_N - t_{41} + t_{44}k_1) & (t_{12}k_N - t_{42}) \\ (t_{31} - t_{34}k_1) & t_{32} \end{vmatrix}}(m_{Bi}e_{Bi}\Omega^2 \mathrm{e}^{j(\Omega t + \beta_{Bi})})$$
$$+ \sum_{No.(Ci)} \frac{\begin{vmatrix} -(q_{12}^{Ci\sim N}k_N - q_{42}^{Ci\sim N}) & (t_{12}k_N - t_{42}) \\ -q_{32}^{Ci\sim N} & t_{32} \end{vmatrix}}{\begin{vmatrix} (t_{11}k_N - t_{14}k_1k_N - t_{41} + t_{44}k_1) & (t_{12}k_N - t_{42}) \\ (t_{31} - t_{34}k_1) & t_{32} \end{vmatrix}}\Delta\alpha_{Ci}(t)$$
$$= \sum_{No.(Bi)} c_{Bi}^U(m_{Bi}e_{Bi}\Omega^2 \mathrm{e}^{j(\Omega t + \beta_{Bi})}) + \sum_{No.(Ci)} c_{Ci}^U \Delta\alpha_{Ci}(t), \tag{17}$$

$$\alpha_1^R = \sum_{No.(Bi)} \frac{\begin{vmatrix} (t_{11}k_N - t_{14}k_1k_N - t_{41} + t_{44}k_1) & -(q_{14}^{Bi\sim N}k_N - q_{44}^{Bi\sim N}) \\ (t_{31} - t_{34}k_1) & -q_{34}^{Bi\sim N} \end{vmatrix}}{\begin{vmatrix} (t_{11}k_N - t_{14}k_1k_N - t_{41} + t_{44}k_1) & (t_{12}k_N - t_{42}) \\ (t_{31} - t_{34}k_1) & t_{32} \end{vmatrix}} (m_{Bi}e_{Bi}\Omega^2 e^{j(\Omega t+\beta_{Bi})})$$

$$+ \sum_{No.(Ci)} \frac{\begin{vmatrix} (t_{11}k_N - t_{14}k_1k_N - t_{41} + t_{44}k_1) & -(q_{12}^{Ci\sim N}k_N - q_{42}^{Ci\sim N}) \\ (t_{31} - t_{34}k_1) & -q_{32}^{Ci\sim N} \end{vmatrix}}{\begin{vmatrix} (t_{11}k_N - t_{14}k_1k_N - t_{41} + t_{44}k_1) & (t_{12}k_N - t_{42}) \\ (t_{31} - t_{34}k_1) & t_{32} \end{vmatrix}} \Delta\alpha_{Ci}(t)$$

$$= \sum_{No.(Bi)} c_{Bi}^\alpha (m_{Bi}e_{Bi}\Omega^2 e^{j(\Omega t+\beta_{Bi})}) + \sum_{No.(Ci)} c_{Ci}^\alpha \Delta\alpha_{Ci}(t), \tag{18}$$

where t_{ij} and $q_{ij}^{r\sim s}$ indicate the (i,j)th elements of the matrices T and $Q^{r\sim s}$, respectively.

The state vector at the measuring station of node number Mi is expressed as follows:

$$\{s\}_{Mi} = Q^{1\sim Mi}\{s\}_1^R + \sum_{No.(Bi)} Q^{Bi\sim Mi}\{u\}_{Bi} + \sum_{No.(Ci)} Q^{Ci\sim Mi}\{c\}_{Ci}. \tag{19}$$

The summation on the right-hand side of Eq. (19) is effective for the unbalance (or balancing) planes only having node numbers smaller than the node number of the measuring plane, i.e., for $Bi < Mi$. Also, the crack position at a node number smaller than the node number of the measuring plane ($Ci < Mi$) is active.

The displacement U_{Mi} at the measuring station is extracted from Eq. (19) as follows:

$$U_{Mi} = \sum_{No.(Bi)} \{(q_{11}^{1\sim Mi} - q_{14}^{1\sim Mi}k_1)c_{Bi}^U + q_{12}^{1\sim Mi}c_{Bi}^\alpha + q_{14}^{Bi\sim Mi}\}(m_{Bi}e_{Bi}\Omega^2 e^{j(\Omega t+\beta_{Bi})})$$

$$+ \sum_{No.(Ci)} \{(q_{11}^{1\sim Mi} - q_{14}^{1\sim Mi}k_1)c_{Ci}^U + q_{12}^{1\sim Mi}c_{Ci}^\alpha + q_{12}^{Ci\sim Mi}\}\Delta\alpha_{Ci}(t). \tag{20}$$

The term $\{(q_{11}^{1\sim Mi} - q_{14}^{1\sim Mi}k_1)c_{Bi}^U + q_{12}^{1\sim Mi}c_{Bi}^\alpha + q_{14}^{Bi\sim Mi}\}$ on the right-hand side of the equation is the influence coefficient, which indicates the relation between the displacement at Mi node and the unbalance at Bi node. Also, the term $\{(q_{11}^{1\sim Mi} - q_{14}^{1\sim Mi}k_1)c_{Ci}^U + q_{12}^{1\sim Mi}c_{Ci}^\alpha + q_{12}^{Ci\sim Mi}\}$ indicates the influence coefficient relating the displacement at the Mi node and the crack breathing at the Ci node. The response depends on the magnitude and phase of each unbalances and the time-dependent breathing behavior of each crack.

4.2. Quasi-static gravity response

The state vector and transfer matrix for the static gravity response are explained in Appendix B. Applying the state vector relations to the step change and crack locations, respectively, yields

$$\begin{aligned} \{s_g\}_i^R &= \{s_g\}_i^L, \\ \{s_g\}_i^R &= \{s_g\}_i^L + \{c\}_i, \end{aligned} \tag{21}$$

where the subscript g indicates the gravity response. The equation amalgamating the state vectors from the first node to the final node N is expressed as follows:

$$\{s_g\}_N^L = T_g\{s_g\}_1^R + (Q_g^{2\sim N}\{g\}_1 + Q_g^{3\sim N}\{g\}_2 + \cdots + Q_g^{(N-1)\sim N}\{g\}_{N-2} + Q_g^{N\sim N}\{g\}_{N-1})e^{j(\pi/2)}$$

$$+ Q_g^{C1\sim N}\{c\}_{C1} + Q_g^{C2\sim N}\{c\}_{C2} + \cdots, \tag{22}$$

where

$$
\{s_g\}_N^L = \left\{ \begin{array}{c} U_{g,N}^L \\ \alpha_{g,N}^L \\ 0 \\ k_N U_{g,N}^L \end{array} \right\}, \quad \{s_g\}_1^R = \left\{ \begin{array}{c} U_{g,1}^R \\ \alpha_{g,1}^R \\ 0 \\ -k_1 U_{g,1}^R \end{array} \right\}, \quad \{g\}_i = \left\{ \begin{array}{c} \dfrac{\rho A_i g l_i^4}{24EI} \\ \dfrac{\rho A_i g l_i^3}{6EI} \\ \dfrac{\rho A_i g l_i^2}{2} \\ \rho A_i g l_i \end{array} \right\}, \quad \{c\}_{Ci} = \left\{ \begin{array}{c} 0 \\ \Delta\alpha_{Ci} \\ 0 \\ 0 \end{array} \right\},
$$

$$
T_g = [F_g]_{N-1}[F_g]_{N-2}\cdots[F_g]_1, \quad Q_g^{m-N} = [F_g]_{N-1}\cdots[F_g]_m, \quad Q_g^{(N-1)-N} = [F_g]_{N-1} \text{ and is the identity matrix.}
$$

If a disk is located at node j, the vector $\{g\}_{j-1}$ in Eq. (22) is replaced by $(\{g\}_{j-1} + \{d_g\}_j)$. In order to give such flexibility, $\{g\}_{j-1}$ is replaced by $\{g\}'_{j-1}$.

For example, if $N = 4$, Eq. (22) becomes

$$
\{s_g\}_4^L = T_g\{s_g\}_1^R + (Q_g^{2\sim4}\{g\}_1 + Q_g^{3\sim4}\{g\}_2 + Q_g^{4\sim4}\{g\}_3)e^{j\pi/2} \tag{23}
$$

and if a disk exists at node 3, the above equation becomes

$$
\{s_g\}_4^L = T_g\{s_g\}_1^R + (Q_g^{2\sim4}\{g\}_1 + Q_g^{3\sim4}(\{g\}_2 + \{d_g\}_3) + Q_g^{4\sim4}\{g\}_3)e^{j\pi/2}. \tag{24}
$$

Solving for the $U_{g,1}^R$ and $\alpha_{g,1}^R$ from Eq. (22), we obtain

$$
U_{g,1}^R = \frac{\left| \begin{array}{cc} -\left(\displaystyle\sum_{i=1}^{N-1} \left\{ \begin{array}{c} (q_{g,11}^{(i+1)\sim N}k_N - q_{g,41}^{(i+1)\sim N}) \\ (q_{g,12}^{(i+1)\sim N}k_N - q_{g,42}^{(i+1)\sim N}) \\ (q_{g,13}^{(i+1)\sim N}k_N - q_{g,43}^{(i+1)\sim N}) \\ (q_{g,14}^{(i+1)\sim N}k_N - q_{g,44}^{(i+1)\sim N}) \end{array} \right\}^{\mathrm{T}} \{g\}'_i \right) & (t_{g,12}k_N - t_{g,42}) \\[4ex] -\left(\displaystyle\sum_{i=1}^{N-1} \left\{ \begin{array}{c} q_{g,31}^{(i+1)\sim N} \\ q_{g,32}^{(i+1)\sim N} \\ q_{g,33}^{(i+1)\sim N} \\ q_{g,34}^{(i+1)\sim N} \end{array} \right\}^{\mathrm{T}} \{g\}'_i \right) & t_{g,32} \end{array} \right|}{\left| \begin{array}{cc} (t_{g,11}k_N - t_{g,14}k_1 k_N - t_{g,41} + t_{g,44}k_1) & (t_{g,12}k_N - t_{g,42}) \\ (t_{g,31} - t_{g,34}k_1) & t_{g,32} \end{array} \right|} e^{j(\pi/2)}
$$

$$
+ \sum_{No.(Ci)} \frac{\left| \begin{array}{cc} -(k_N q_{g,12}^{Ci\sim N} - q_{g,42}^{Ci\sim N}) & (t_{g,12}k_N - t_{g,42}) \\ -q_{g,32}^{Ci\sim N} & t_{g,32} \end{array} \right|}{\left| \begin{array}{cc} (t_{g,11}k_N - t_{g,14}k_1 k_N - t_{g,41} + t_{g,44}k_1) & (t_{g,12}k_N - t_{g,42}) \\ (t_{g,31} - t_{g,34}k_1) & t_{g,32} \end{array} \right|} \Delta\alpha_{Ci}
$$

$$
= \sum_{i=1}^{N-1} c_{g,i}^U \{g\}'_j e^{j(\pi/2)} + \sum_{No.(Ci)} c_{g,Ci}^U \Delta\alpha_{Ci}, \tag{25}
$$

$$\alpha_{g,1}^{R} = \frac{\begin{vmatrix} (t_{g,11}k_N - t_{g,14}k_1 k_N - t_{g,41} + t_{g,44}k_1) & -\left(\sum_{i=1}^{N-1}\begin{Bmatrix} (q_{g,11}^{(i+1)\sim N}k_N - q_{g,41}^{(i+1)\sim N}) \\ (q_{g,12}^{(i+1)\sim N}k_N - q_{g,42}^{(i+1)\sim N}) \\ (q_{g,13}^{(i+1)\sim N}k_N - q_{g,43}^{(i+1)\sim N}) \\ (q_{g,14}^{(i+1)\sim N}k_N - q_{g,44}^{(i+1)\sim N}) \end{Bmatrix}^{\mathrm{T}}\{g\}'_j\right) \\ (t_{g,31} - t_{g,34}k_1) & \left(-\sum_{i=1}^{N-1}\begin{Bmatrix} q_{g,31}^{(i+1)\sim N} \\ q_{g,32}^{(i+1)\sim N} \\ q_{g,33}^{(i+1)\sim N} \\ q_{g,34}^{(i+1)\sim N} \end{Bmatrix}^{\mathrm{T}}\{g\}'_j\right) \end{vmatrix}}{\begin{vmatrix} (t_{g,11}k_N - t_{g,14}k_1 k_N - t_{g,41} + t_{g,44}k_1) & (t_{g,12}k_N - t_{g,42}) \\ (t_{g,31} - t_{g,34}k_1) & t_{g,32} \end{vmatrix}} e^{j(\pi/2)}$$

$$+ \sum_{No.(Ci)} \frac{\begin{vmatrix} (t_{g,11}k_N - t_{g,14}k_1 k_N - t_{g,41} + t_{g,44}k_1) & -(k_N q_{g,12}^{Ci\sim N} - q_{g,42}^{Ci\sim N}) \\ (t_{g,31} - t_{g,34}k_1) & -q_{g,32}^{Ci\sim N} \end{vmatrix}}{\begin{vmatrix} (t_{g,11}k_N - t_{g,14}k_1 k_N - t_{g,41} + t_{g,44}k_1) & (t_{g,12}k_N - t_{g,42}) \\ (t_{g,31} - t_{g,34}k_1) & t_{g,32} \end{vmatrix}} \Delta\alpha_{Ci}$$

$$= \sum_{i=1}^{N-1} c_{g,i}^{\alpha}\{g\}'_j e^{j(\pi/2)} + \sum_{No.(Ci)} c_{g,Ci}^{\alpha}\Delta\alpha_{Ci}, \tag{26}$$

where $q_{g,ij}^{r\sim s}$ and $t_{g,ij}$ denote the (i,j) element of $Q_g^{r\sim s}$ and T_g matrices, respectively. Each of the first terms of the right-hand sides of Eqs. (25) and (26) is related to the static deflection of the shaft due to the gravitational force, and the second term of the equations is related to the additional deflection due to crack breathing. However, this additional deflection includes the quasi-static behavior only, excluding the dynamic effect.

The state vector at the measuring station of node number Mi is expressed as follows:

$$\{s_g\}_{Mi}^{L} = Q_g^{1\sim Mi}\{s_g\}_1^{R} + (Q_g^{2\sim Mi}\{g\}'_1 + Q_g^{3\sim Mi}\{g\}'_2 + \cdots + Q_g^{(Mi-1)\sim Mi}\{g\}'_{Mi-2} + Q_g^{Mi\sim Mi}\{g\}'_{Mi-1})e^{j(\pi/2)}$$
$$+ Q_g^{C1\sim Mi}\{c\}_{C1} + Q_g^{C2\sim Mi}\{c\}_{C2} + \cdots . \tag{27}$$

The displacement $U_{g,Mi}$ at the measuring station is extracted from Eq. (27) as follows:

$$U_{g,Mi} = \sum_{i=1}^{N-1}\left((q_{g,11}^{1\sim Mi} - q_{g,14}^{1\sim Mi}k_1)c_{g,i}^{U} + q_{g,12}^{1\sim Mi}c_{g,i}^{\alpha}\right)\{g\}'_j e^{j(\pi/2)} + \left(\sum_{i=1}^{Mi-1}\begin{Bmatrix} q_{g,11}^{(i+1)\sim Mi} \\ q_{g,12}^{(i+1)\sim Mi} \\ q_{g,13}^{(i+1)\sim Mi} \\ q_{g,14}^{(i+1)\sim Mi} \end{Bmatrix}^{\mathrm{T}}\{g\}'_j\right)e^{j(\pi/2)}$$

$$+ \sum_{No.(Ci)}\left((q_{g,11}^{1\sim Mi} - q_{g,14}^{1\sim Mi}k_1)c_{g,Ci}^{U} + q_{g,12}^{1\sim Mi}c_{g,Ci}^{\alpha}\right)\Delta\alpha_{Ci} + \sum_{Ci=C1}^{Mi} q_{g,12}^{Ci\sim Mi}\Delta\alpha_{Ci}. \tag{28}$$

The crack position at a node number smaller than the node number of the measuring plane ($Ci < Mi$) is active in the last term of the above equation.

5. Cracked rotor analysis method

5.1. Iterative procedure

The bending moment around a crack position directly influences on the crack opening status as discussed above. In Fig. 4 is shown the bending moments expressed in the rotating coordinates. Using the given notation, negative M_η yields positive $K^I_{M_\eta}$ on the crack front and also negative M_ξ yields positive $K^I_{M_\xi}$ on the crack front on the positive η axis. The bending moment on the rotating coordinates is obtained by transforming the bending moment on the stationary coordinates as follows:

$$M_\eta + jM_\xi = (M_z + jM_y)e^{-j\Omega t} \tag{29}$$

from

$$\begin{Bmatrix} y+jz \\ \phi+j\theta \\ M_z+jM_y \\ V_y+jV_z \end{Bmatrix} = \begin{Bmatrix} \xi+j\eta \\ \phi_\eta+j\theta_\xi \\ M_\eta+jM_\xi \\ V_\xi+jV_\eta \end{Bmatrix} e^{j\Omega t}, \tag{30}$$

where the bending moment (M_z+jM_y) on the stationary coordinates is obtained by summing the bending moment at the crack node from the dynamic response and that from the static gravity response. The bending moment in the rotating coordinates is used for estimation of the additional slope at the crack location by using the method discussed in Section 3.

The state vectors at a node with a crack corresponding to the dynamic response and static gravity response are expressed as follows, respectively (note that subscript c indicates the node number with a crack):

$$\{s\}_C = Q^{1\sim C}\{s\}^R_1 + \sum_{No.(Bi)} Q^{Bi\sim C}\{u\}_{Bi} + \sum_{No.(Ci)} Q^{Ci\sim C}\{c\}_{Ci}, \tag{31}$$

$$\{s_g\}^L_C = Q^{1\sim C}_g\{s_g\}^R_1 + (Q^{2\sim C}_g\{g\}'_1 + Q^{3\sim C}_g\{g\}'_2 + \cdots + Q^{(C-1)\sim C}_g\{g\}'_{c-2} + Q^{C\sim C}_g\{g\}'_{c-1}) \cdot e^{j(\pi/2)}$$
$$+ Q^{C1\sim C}_g\{c\}_{C1} + Q^{C2\sim C}_g\{c\}_{C2} + \cdots . \tag{32}$$

The summations on the right-hand side of Eq. (31) are effective for the unbalance and for the cracks having node numbers smaller than the node number of the current node with a crack, i.e., for $Bi < C$ and $Ci < C$, respectively.

From the above equations the bending moments related to the dynamic response and the static gravity response, respectively, are extracted as follows:

$$M_C = \sum_{No.(Bi)} \{(q^{1\sim C}_{31} - q^{1\sim C}_{34}k_1)c^U_{Bi} + q^{1\sim C}_{32}c^\alpha_{Bi} + q^{Bi\sim C}_{34}\}(m_{Bi}e_{Bi}\Omega^2 e^{j(\Omega t+\beta_{Bi})})$$
$$+ \sum_{Ci=C1}^{C} \{(q^{1\sim C}_{31} - q^{1\sim C}_{34}k_1)c^U_{Ci} + q^{1\sim C}_{32}c^\alpha_{Ci} + q^{Ci\sim C}_{32}\} \quad \Delta\alpha_{Ci}(t), \tag{33}$$

$$M_{g,C} = (q^{1\sim C}_{g,31} - q^{1\sim C}_{g,34}k_1)U^R_{g,1} + q^{1\sim C}_{g,32}\alpha^R_{g,1} + \left(\sum_{i=1}^{C-1} \begin{Bmatrix} q^{(i+1)\sim C}_{g,31} \\ q^{(i+1)\sim C}_{g,32} \\ q^{(i+1)\sim C}_{g,33} \\ q^{(i+1)\sim C}_{g,34} \end{Bmatrix}^{\mathrm{T}} \{g\}'_j\right)e^{j(\pi/2)} + \sum_{Ci=C1}^{C} q^{Ci\sim C}_{g,32}\Delta\alpha_{Ci}. \tag{34}$$

The crack opening status is determined by the bending moment in the region of the crack, which is one of the state variables and it is affected by the crack opening status as shown in Eqs. (33) and (34). Thus, the two parameters are coupled. For analysis of the motion, the following iterative procedure is introduced.

5.2. Consideration of harmonic components—parametrically excited forcing functions

If one crack is considered for simplicity, the total bending moment at crack position is expressed as follows:

$$
\begin{aligned}
M_C = {} & \sum_{No.(Bi)} \left\{ (q_{31}^{1\sim C} - q_{34}^{1\sim C} k_1) c_{Bi}^U + q_{32}^{1\sim C} c_{Bi}^\alpha + q_{34}^{Bi\sim C} \right\} (m_{Bi} e_{Bi} \Omega^2 e^{j(\Omega t + \beta_{Bi})}) \\
& + \left\{ (q_{31}^{1\sim C} - q_{34}^{1\sim C} k_1) c_C^U + q_{32}^{1\sim C} c_C^\alpha \right\} \Delta \alpha_C(t) \\
& + \sum_{i=1}^{N-1} \left((q_{g,31}^{1\sim C} - q_{g,34}^{1\sim C} k_1) c_{g,i}^U + q_{g,32}^{1\sim C} c_{g,i}^\alpha \right) \{g\}_j' e^{j(\pi/2)} + \left(\sum_{i=1}^{C-1} \begin{Bmatrix} q_{g,31}^{(i+1)\sim C} \\ q_{g,32}^{(i+1)\sim C} \\ q_{g,33}^{(i+1)\sim C} \\ q_{g,34}^{(i+1)\sim C} \end{Bmatrix}^{\mathrm{T}} \{g\}_j' \right) e^{j(\pi/2)} \\
& + \sum_{No.(Ci)} \left((q_{g,31}^{1\sim C} - q_{g,34}^{1\sim C} k_1) c_{g,C}^U + q_{g,32}^{1\sim C} c_{g,C}^\alpha \right) \Delta \alpha_C(t).
\end{aligned}
\tag{35}
$$

However, the last term of the gravity-related terms in Eq. (35), which is related the crack breathing, disappears because all components $q_{g,ij}^{r\sim s}$ and accordingly $c_{g,C}^U$ have zero value when $i > j$. Thus, the bending moment depending on the crack breathing exists in a dynamic response term. The bending moment consists of the unbalance- and crack breathing-related terms, which are derived from dynamic response, and the terms related to the quasi-static deflection due to gravity.

The behavior of cracked rotor is generally nonlinear one with response-dependent nonlinear stiffness terms. However, each term in Eq. (35) represents a linear influence coefficient (or transfer function) relating the bending moment to each source of rotor motion. The nonlinear behavior is produced by self-excitation, which is the additional slope at a node with crack, $\Delta \alpha_c(t)$. In this study the crack breathing-related term, which is the cause of nonlinear vibration, is expressed explicitly in the equation. When a rotor rotates with a constant speed, the additional slope produces the harmonic vibration components, which are caused by the transient motion during crack breathing.

In order to consider the harmonic motion, the additional slope due to crack breathing is expressed as the sum of harmonics as follows:

$$
\Delta \alpha_C(t) = \sum_{n=-\infty}^{\infty} c_n e^{j\Omega_n t},
\tag{36}
$$

where $\Omega_n = n\Omega$ and the coefficient

$$
c_n = \frac{\Omega}{2\pi} \int_{-\pi/\Omega}^{\pi/\Omega} \Delta \alpha_3(t) e^{-j\Omega_n t} \, dt.
$$

Rewriting Eq. (35) in function form, we have

$$
\begin{aligned}
M_C = {} & F_C(\Omega) \Delta \alpha_3(t) + F_U(\Omega) e^{j\Omega t} + F_g \\
= {} & \cdots + F_C(\Omega_{-3}) c_{-3} e^{j\Omega_{-3} t} + F_C(\Omega_{-2}) c_{-2} e^{j\Omega_{-2} t} + F_C(\Omega_{-1}) c_{-1} e^{j\Omega_{-1} t} \\
& + F_C(\Omega_0) c_0 + F_g \\
& + \left(F_C(\Omega) c_{+1} + \sum_{No.(Bi)} F_U(\Omega) \right) e^{j\Omega t} \\
& + F_C(\Omega_2) c_{+2} e^{j\Omega_2 t} + F_C(\Omega_3) c_{+3} e^{j\Omega_3 t} + \cdots,
\end{aligned}
\tag{37}
$$

where

$$
F_C(\Omega) = (q_{31}^{1\sim C} - q_{34}^{1\sim C} k_1) c_C^U + q_{32}^{1\sim C} c_C^\alpha,
\tag{38}
$$

$$F_U(\Omega) = \left((q_{31}^{1\sim C} - q_{34}^{1\sim C}k_1)c_{Bi}^U + q_{32}^{1\sim C}c_{Bi}^{\alpha} + q_{34}^{Bi\sim C}\right)m_{Bi}e_{Bi}\Omega^2 e^{j\beta_{Bi}}, \tag{39}$$

$$F_g = \sum_{i=1}^{N-1}\left((q_{g,31}^{1\sim C} - q_{g,34}^{1\sim C}k_1)c_{g,i}^U + q_{g,32}^{1\sim C}c_{g,i}^{\alpha}\right)\{g\}'_j e^{j(\pi/2)} + \left(\sum_{i=1}^{C-1}\begin{Bmatrix} q_{g,31}^{(i+1)\sim C} \\ q_{g,32}^{(i+1)\sim C} \\ q_{g,33}^{(i+1)\sim C} \\ q_{g,34}^{(i+1)\sim C} \end{Bmatrix}^{\mathrm{T}} \{g\}'_j\right) e^{j(\pi/2)}. \tag{40}$$

In the calculation of the dynamic influence coefficients in Eqs. (38) and (39), the synchronous condition $\omega = \Omega$ is used. The coefficients of the Fourier-series expansion are calculated by using the simulation set for the additional slope $\Delta\alpha_c(t)$, of Eq. (36), for a full revolution. Fourier-series expansion of the additional slope is performed before we calculate the bending moment on the step of the double-lined box in Fig. 9. At each angle step, the new Fourier coefficients are calculated from the additional slope solution set for one revolution of the shaft until the one prior to the angle step. Fig. 10 shows the additional slope solution set of one revolution for the 'moving' Fourier-series expansion.
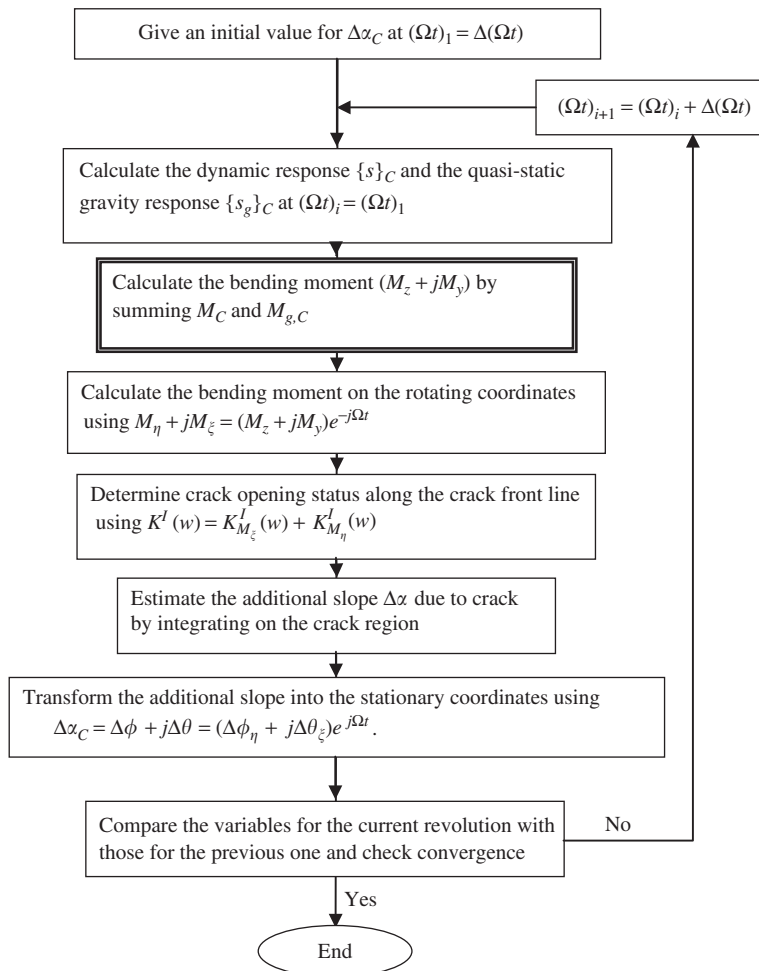

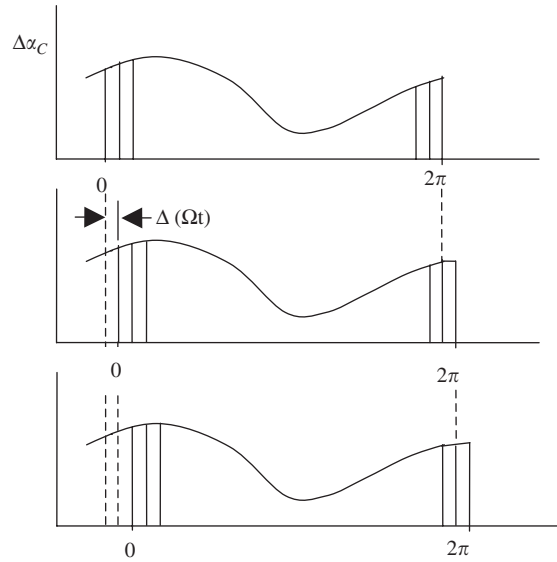Fig. 9. Iterative procedure for cracked rotor analysis.

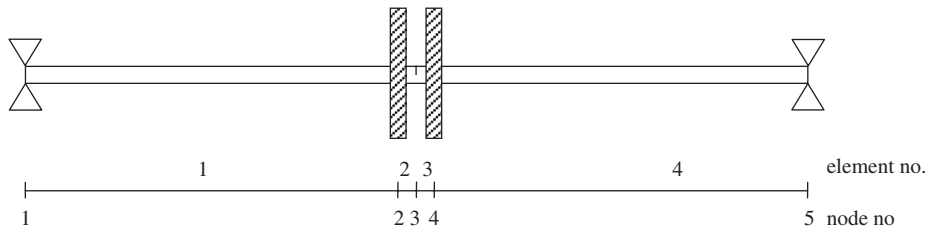Fig. 10. Scheme of 'moving' Fourier-series expansion.

Fig. 11. Simple rotor having a breathing crack. ($E = 2.12\,10\,\mathrm{kg_f/cm^3}$, $\rho = 0.0078\,\mathrm{kg/cm^3}$ and $k = 1\,10^{10}\,\mathrm{N/m}$.)

If we express the newly obtained Fourier coefficients as c'_n, the equation can be rewritten as follows:

$$
\begin{aligned}
M_C = {} & \cdots + F_C(\Omega_{-3})c'_{-3} + F_C(\Omega_{-2})c'_{-2} + F_C(\Omega_{-1})c'_{-1} \\
& + F_g + \sum_{No.(Bi)} F_U(\Omega)\mathrm{e}^{j\Omega t} \\
& + F_C(\Omega)c'_{+1} + F_C(\Omega_2)c'_{+2} + F_C(\Omega_3)c'_{+3} + \cdots .
\end{aligned}
\tag{41}
$$

The constant component of the Fourier expansion is omitted since it is not related to the dynamic behavior.

6. Simulation and discussion

6.1. Modeling

A simple model is used for simulation. The model of Fig. 11 is the same model that was used to simulate a rotor with a breathing crack in Ref. [9]. The shaft diameter is 1.5 cm, total length is 70 cm, and a crack is located at the center of the shaft. The lengths of each shaft element are 33.5, 1.5, 1.5 and 33.5 cm, respectively. Each of the two disks at the mid-span has a mass of 1.4 kg, and the transverse and polar moments of inertia of each disk are 12.8 and 25.6 kg cm^2, respectively.

Introducing the state vector and transfer matrix for the dynamics analysis, the relations between the right-hand side of node 1 and the left-hand side of node 5 are expressed as follows:

$$\{s\}_2^L = [F]_1\{s\}_1^R, \quad \{s\}_2^R = [s]_2\{s\}_2^L + \{u\}_2, \quad \{s\}_3^L = [F]_2\{s\}_2^R, \quad \{s\}_3^R = \{s\}_3^L + \{c\}_3,$$
$$\{s\}_4^L = [F]_3\{s\}_3^R, \quad \{s\}_4^R = [s]_4\{s\}_4^L + \{u\}_4, \quad \{s\}_5^L = [F]_4\{s\}_4^R. \tag{42}$$

The seven expressions above are integrated into one equation as follows:

$$\{s\}_5^L = [F]_4[S]_4[F]_3[F]_2[S]_2[F]_1\{\}_1^R + [F]_4[S]_4[F]_3[F]_2\{u\}_2 + [F]_4[S]_4[F]_3\{c\}_3 + [F]_4\{u\}_4$$
$$= T\{s\}_1^R + Q^{2\sim5}\{u\}_2 + Q^{3\sim5}\{c\}_3 + Q^{4\sim5}\{u\}_4.$$

Considering the boundary conditions at both bearings

$$\{s\}_1^R = \begin{Bmatrix} U_1 \\ \alpha_1 \\ 0 \\ -k_1 U_1 \end{Bmatrix} \quad \text{and} \quad \{s\}_5^L = \begin{Bmatrix} U_5 \\ \alpha_5 \\ 0 \\ k_5 U_5 \end{Bmatrix},$$

we obtain the slope and the shear force at node 1 as follows:

$$U_1^R = c_{B2}^U(m_2 e_2 \Omega^2 e^{j(\Omega t + \beta_2)}) + c_{B4}^U(m_4 e_4 \Omega^2 e^{j(\Omega t + \beta_4)}) + c_{C3}^U \Delta\alpha_3(t),$$

$$\alpha_1^R = c_{B2}^\alpha(m_2 e_2 \Omega^2 e^{j(\Omega t + \beta_2)}) + c_{B4}^\alpha(m_4 e_4 \Omega^2 e^{j(\Omega t + \beta_4)}) + c_{C3}^\alpha \Delta\alpha_3(t),$$

where

$$c_{Bi}^U = \frac{\begin{vmatrix} -(q_{14}^{Ui\sim5}k_N - q_{44}^{Ui\sim5}) & (t_{12}k_N - t_{42}) \\ -q_{34}^{Ui\sim5} & t_{32} \end{vmatrix}}{\begin{vmatrix} (t_{11}k_N - t_{14}k_1 k_N - t_{41} + t_{44}k_1) & (t_{12}k_N - t_{42}) \\ (t_{31} - t_{34}k_1) & t_{32} \end{vmatrix}},$$

$$c_{Ci}^U = \frac{\begin{vmatrix} -(q_{12}^{Ci\sim5}k_N - q_{42}^{Ci\sim5}) & (t_{12}k_N - t_{42}) \\ -q_{32}^{Ci\sim5} & t_{32} \end{vmatrix}}{\begin{vmatrix} (t_{11}k_N - t_{14}k_1 k_N - t_{41} + t_{44}k_1) & (t_{12}k_N - t_{42}) \\ (t_{31} - t_{34}k_1) & t_{32} \end{vmatrix}},$$

$$c_{Bi}^\alpha = \frac{\begin{vmatrix} (t_{11}k_N - t_{14}k_1 k_N - t_{41} + t_{44}k_1) & -(q_{14}^{Ui\sim5}k_N - q_{44}^{Ui\sim5}) \\ (t_{31} - t_{34}k_1) & -q_{34}^{Ui\sim5} \end{vmatrix}}{\begin{vmatrix} (t_{11}k_N - t_{14}k_1 k_N - t_{41} + t_{44}k_1) & (t_{12}k_N - t_{42}) \\ (t_{31} - t_{34}k_1) & t_{32} \end{vmatrix}},$$

$$c_{Ci}^\alpha = \frac{\begin{vmatrix} (t_{11}k_N - t_{14}k_1 k_N - t_{41} + t_{44}k_1) & -(q_{12}^{Ci\sim5}k_N - q_{42}^{Ci\sim5}) \\ (t_{31} - t_{34}k_1) & -q_{32}^{Ci\sim5} \end{vmatrix}}{\begin{vmatrix} (t_{11}k_N - t_{14}k_1 k_N - t_{41} + t_{44}k_1) & (t_{12}k_N - t_{42}) \\ (t_{31} - t_{34}k_1) & t_{32} \end{vmatrix}}.$$

The state vector at node 3 is expressed as follows:

$$\{s\}_3^L = F^{23}S^2F^{12}\{s\}_1^R + F^{23}\{u\}_2$$
$$= Q^{1\sim3}\{s\}_1^R + Q^{2\sim3}\{u\}_2. \tag{43}$$

By using the state vector and transfer matrix for the quasi-static gravity response of Appendix B produces the relations in a form similar to the dynamic response:

$$\{s_g\}_2^L = [F_g]_1\{s_g\}_1^R + \{g\}_1 e^{j(\pi/2)}, \quad \{s_g\}_2^R = \{s_g\}_2^L + \{d_g\}_2 e^{j(\pi/2)}, \quad \{s_g\}_3^L = [F_g]_2\{s_g\}_2^R + \{g\}_2 e^{j(\pi/2)},$$
$$\{s_g\}_3^R = \{s_g\}_3^L + \{c\}_3, \quad \{s_g\}_4^L = [F_g]_3\{s_g\}_3^R + \{g\}_3 e^{j(\pi/2)}, \quad \{s_g\}_4^R = \{s_g\}_4^L + \{d_g\}_4 e^{j(\pi/2)},$$
$$\{s_g\}_5^L = [F_g]_4\{s_g\}_4^R + \{g\}_4 e^{j(\pi/2)}. \tag{44}$$

The above seven expressions are integrated into one equation as follows:

$$\{s_g\}_5^L = [F_g]_4[F_g]_3[F_g]_2[F_g]_1\{s_g\}_1^R + [F_g]_4[F_g]_3[F_g]_2(\{g\}_1 + \{d_g\}_2)e^{j(\pi/2)}$$
$$+ [F_g]_4[F_g]_3\{g\}_2 e^{j(\pi/2)} + [F_g]_4[F_g]_3\{c\}_3 + [F_g]_4(\{g\}_3 + \{d_g\}_4)e^{j(\pi/2)} + \{g\}_4 e^{j(\pi/2)}$$
$$= T_g\{s_g\}_1^R + (Q_g^{2\sim5}(\{g\}_1 + \{d_g\}_2) + Q_g^{3\sim5}\{g\}_2 + Q_g^{4\sim5}(\{g\}_3 + \{d_g\}_4) + \{g\}_4)e^{j(\pi/2)} + Q_g^{3\sim5}\{c\}_3.$$

The boundary conditions at both bearings are expressed for the quasi-static gravity response as follows:

$$\{s_g\}_1^R = \begin{Bmatrix} U_{g,1} \\ \alpha_{g,1} \\ 0 \\ -k_1 U_{g,1} \end{Bmatrix} \quad \text{and} \quad \{s_g\}_5^L = \begin{Bmatrix} U_{g,5} \\ \alpha_{g,5} \\ 0 \\ k_5 U_{g,5} \end{Bmatrix}.$$

Solving for $U_{g,1}^R$ and $\alpha_{g,1}^R$ yields

$$U_{g,1}^R = \frac{\begin{vmatrix} -\left(\sum_{i=1}^{4} \begin{Bmatrix} (q_{g,11}^{(i+1)\sim5}k_5 - q_{g,41}^{(i+1)\sim5}) \\ (q_{g,12}^{(i+1)\sim5}k_5 - q_{g,42}^{(i+1)\sim5}) \\ (q_{g,13}^{(i+1)\sim5}k_5 - q_{g,43}^{(i+1)\sim5}) \\ (q_{g,14}^{(i+1)\sim5}k_5 - q_{g,44}^{(i+1)\sim5}) \end{Bmatrix}^{\mathrm{T}} \{g\}_i' \right) & (t_{g,12}k_5 - t_{g,42}) \\ -\left(\sum_{i=1}^{4} \begin{Bmatrix} q_{g,31}^{(i+1)\sim5} \\ q_{g,32}^{(i+1)\sim5} \\ q_{g,33}^{(i+1)\sim5} \\ q_{g,34}^{(i+1)\sim5} \end{Bmatrix}^{\mathrm{T}} \{g\}_i' \right) & t_{g,32} \end{vmatrix}}{\begin{vmatrix} (t_{g,11}k_5 - t_{g,14}k_1k_5 - t_{g,41} + t_{g,44}k_1) & (t_{g,12}k_5 - t_{g,42}) \\ (t_{g,31} - t_{g,34}k_1) & t_{g,32} \end{vmatrix}} e^{j(\pi/2)}$$
$$+ \frac{\begin{vmatrix} -(q_{g,12}^{3\sim5}k_5 - q_{g,42}^{3\sim5}) & (t_{g,12}k_5 - t_{g,42}) \\ -q_{g,32}^{3\sim5} & t_{g,32} \end{vmatrix}}{\begin{vmatrix} (t_{g,11}k_5 - t_{g,14}k_1k_5 - t_{g,41} + t_{g,44}k_1) & (t_{g,12}k_5 - t_{g,42}) \\ (t_{g,31} - t_{g,34}k_1) & t_{g,32} \end{vmatrix}} \Delta\alpha_3$$

$$
\alpha_{g,1}^R = \frac{
\begin{vmatrix}
(t_{g,11}k_5 - t_{g,14}k_1k_5 - t_{g,41} + t_{g,44}k_1) & -\left(\sum\limits_{i=1}^{4} \begin{Bmatrix} (q_{g,11}^{(i+1)\sim5}k_5 - q_{g,41}^{(i+1)\sim5}) \\ (q_{g,12}^{(i+1)\sim5}k_5 - q_{g,42}^{(i+1)\sim5}) \\ (q_{g,13}^{(i+1)\sim5}k_5 - q_{g,43}^{(i+1)\sim5}) \\ (q_{g,14}^{(i+1)\sim5}k_5 - q_{g,44}^{(i+1)\sim5}) \end{Bmatrix}^{\mathrm{T}} \{g\}'_i \right) \\
(t_{g,31} - t_{g,34}k_1) & -\left(\sum\limits_{i=1}^{4} \begin{Bmatrix} q_{g,31}^{(i+1)\sim5} \\ q_{g,32}^{(i+1)\sim5} \\ q_{g,33}^{(i+1)\sim5} \\ q_{g,34}^{(i+1)\sim5} \end{Bmatrix}^{\mathrm{T}} \{g\}'_i \right)
\end{vmatrix}
}{
\begin{vmatrix}
(t_{g,11}k_5 - t_{g,14}k_1k_5 - t_{g,41} + t_{g,44}k_1) & (t_{g,12}k_5 - t_{g,42}) \\
(t_{g,31} - t_{g,34}k_1) & t_{g,32}
\end{vmatrix}
} e^{j(\pi/2)}
$$

$$
+ \frac{
\begin{vmatrix}
(t_{g,11}k_5 - t_{g,14}k_1k_5 - t_{g,41} + t_{g,44}k_1) & -(q_{g,12}^{3\sim5}k_5 - q_{g,42}^{3\sim5}) \\
(t_{g,31} - t_{g,34}k_1) & -q_{g,32}^{3\sim5}
\end{vmatrix}
}{
\begin{vmatrix}
(t_{g,11}k_5 - t_{g,14}k_1k_5 - t_{g,41} + t_{g,44}k_1) & (t_{g,12}k_5 - t_{g,42}) \\
(t_{g,31} - t_{g,34}k_1) & t_{g,32}
\end{vmatrix}
} \Delta\alpha_3,
$$

where

$$
\{g\}'_1 = \{g\}_1 + \{d_g\}_2, \quad \{g\}'_2 = \{g\}_2, \quad \{g\}'_3 = \{g\}_3 + \{d_g\}_4 \quad \text{and} \quad \{g\}'_4 = \{g\}_4.
$$

The above equations for $U_{g,1}^R$ and $\alpha_{g,1}^R$ are rewritten as follows:

$$
U_{g,1}^R = \sum_{i=1}^{4} c_{g,i}^U \{g\}'_i e^{j(\pi/2)} + c_{g,C3}^U \Delta\alpha_3(t),
$$

$$
\alpha_{g,1}^R = \sum_{i=1}^{4} c_{g,i}^\alpha \{g\}'_i e^{j(\pi/2)} + c_{g,C3}^\alpha \Delta\alpha_3(t),
$$

where

$$
c_{g,i}^U = \frac{
-\left(\begin{Bmatrix} t_{g,32} \begin{Bmatrix} (q_{g,11}^{(i+1)\sim5}k_5 - q_{g,41}^{(i+1)\sim5}) \\ (q_{g,12}^{(i+1)\sim5}k_5 - q_{g,42}^{(i+1)\sim5}) \\ (q_{g,13}^{(i+1)\sim5}k_5 - q_{g,43}^{(i+1)\sim5}) \\ (q_{g,14}^{(i+1)\sim5}k_5 - q_{g,44}^{(i+1)\sim5}) \end{Bmatrix} - (t_{g,12}k_5 - t_{g,42}) \begin{Bmatrix} q_{g,31}^{(i+1)\sim5} \\ q_{g,32}^{(i+1)\sim5} \\ q_{g,33}^{(i+1)\sim5} \\ q_{g,34}^{(i+1)\sim5} \end{Bmatrix} \end{Bmatrix} \right)^{\mathrm{T}}
}{
\begin{vmatrix}
(t_{g,11}k_5 - t_{g,14}k_1k_5 - t_{g,41} + t_{g,44}k_1) & (t_{g,12}k_5 - t_{g,42}) \\
(t_{g,31} - t_{g,34}k_1) & t_{g,32}
\end{vmatrix}
},
$$

$$
c_{g,C3}^U = \frac{
\begin{vmatrix}
-(q_{g,12}^{3\sim5}k_5 - q_{g,42}^{3\sim5}) & (t_{g,12}k_5 - t_{g,42}) \\
-q_{g,32}^{3\sim5} & t_{g,32}
\end{vmatrix}
}{
\begin{vmatrix}
(t_{g,11}k_5 - t_{g,14}k_1k_5 - t_{g,41} + t_{g,44}k_1) & (t_{g,12}k_5 - t_{g,42}) \\
(t_{g,31} - t_{g,34}k_1) & t_{g,32}
\end{vmatrix}
},
$$

$$c_{g,i}^{\alpha} = \cfrac{-\left((t_{g,11}k_5 - t_{g,14}k_1k_5 - t_{g,41} + t_{g,44}k_1) \begin{Bmatrix} q_{g,31}^{(i+1)\sim5} \\ q_{g,32}^{(i+1)\sim5} \\ q_{g,33}^{(i+1)\sim5} \\ q_{g,34}^{(i+1)\sim5} \end{Bmatrix} - (t_{g,31} - t_{g,34}k_1) \begin{Bmatrix} (q_{g,11}^{(i+1)\sim5}k_5 - q_{g,41}^{(i+1)\sim5}) \\ (q_{g,12}^{(i+1)\sim5}k_5 - q_{g,42}^{(i+1)\sim5}) \\ (q_{g,13}^{(i+1)\sim5}k_5 - q_{g,43}^{(i+1)\sim5}) \\ (q_{g,14}^{(i+1)\sim5}k_5 - q_{g,44}^{(i+1)\sim5}) \end{Bmatrix} \right)^{\mathrm{T}}}{\begin{vmatrix} (t_{g,11}k_5 - t_{g,14}k_1k_5 - t_{g,41} + t_{g,44}k_1) & (t_{g,12}k_5 - t_{g,42}) \\ (t_{g,31} - t_{g,34}k_1) & t_{g,32} \end{vmatrix}},$$

$$c_{g,C3}^{\alpha} = \cfrac{\begin{vmatrix} (t_{g,11}k_5 - t_{g,14}k_1k_5 - t_{g,41} + t_{g,44}k_1) & -(q_{g,12}^{3\sim5}k_5 - q_{g,42}^{3\sim5}) \\ (t_{g,31} - t_{g,34}k_1) & -q_{g,32}^{3\sim5} \end{vmatrix}}{\begin{vmatrix} (t_{g,11}k_5 - t_{g,14}k_1k_5 - t_{g,41} + t_{g,44}k_1) & (t_{g,12}k_5 - t_{g,42}) \\ (t_{g,31} - t_{g,34}k_1) & t_{g,32} \end{vmatrix}}.$$

The state vector at node 3 is expressed as follows:

$$\{s_g\}_3^L = Q_g^{1\sim3}\{s_g\}_1^R + (Q_g^{2\sim3}\{g\}'_i + Q_g^{3\sim3}\{g\}_2)e^{j(\pi/2)}. \tag{45}$$

Extracting the bending moments from the Eqs. (43) and (45), the total bending moment is expressed in the form of Eqs. (38)–(41):

$$\begin{aligned} M_3 = \cdots &+ F_C(\Omega_{-3})c'_{-3} + F_C(\Omega_{-2})c'_{-2} + F_C(\Omega_{-1})c'_{-1} \\ &+ F_g + F_{U,2}(\Omega)e^{j\Omega t} + F_{U,4}(\Omega)e^{j\Omega t} \\ &+ F_C(\Omega)c'_{+1} + F_C(\Omega_2)c'_{+2} + F_C(\Omega_3)c'_{+3} + \cdots, \end{aligned} \tag{46}$$

where

$$F_C(\Omega) = ((q_{31}^{1\sim3} - q_{34}^{1\sim3}k_1)c_{C3}^U + q_{32}^{1\sim3}c_{C3}^{\alpha}),$$
$$F_{U,2}(\Omega) = ((q_{31}^{1\sim3} - q_{34}^{1\sim3}k_1)c_{B2}^U + q_{32}^{1\sim3}c_{B2}^{\alpha} + q_{32}^{2\sim3})m_2e_2\Omega^2 e^{j\beta_2},$$
$$F_{U,4}(\Omega) = ((q_{31}^{1\sim3} - q_{34}^{1\sim3}k_1)c_{B4}^U + q_{32}^{1\sim3}c_{B4}^{\alpha})m_4e_4\Omega^2 e^{j\beta_4},$$

$$F_g = \sum_{i=1}^{4}\left((q_{g,31}^{1\sim3} - q_{g,34}^{1\sim3}k_1)c_{g,i}^U + q_{g,32}^{1\sim3}c_{g,i}^{\alpha}\right)\{g\}'_i e^{j(\pi/2)} + \left(\sum_{i=1}^{2}\begin{Bmatrix} q_{g,31}^{(i+1)\sim3} \\ q_{g,32}^{(i+1)\sim3} \\ q_{g,33}^{(i+1)\sim3} \\ q_{g,34}^{(i+1)\sim3} \end{Bmatrix}^{\mathrm{T}} \{g\}'_i\right)e^{j(\pi/2)}.$$

6.2. Results and discussion

The bearing stiffness is assumed to be a large value of 1.0×10^{10} N/m, in order to compare the simulation with the previous study which used rigid bearings [9]. The influence coefficient [20] between unbalance force at node 2 (input) and displacement at node 3 (output), from Eq. (20), is calculated and plotted as shown in Fig. 12. This model has the first three critical speeds at 149, 2590 and 8490 rad/s when there is no crack.

The previous study in Ref. [9] used a simple rotor model composed of a massless shaft and a lumped mass at mid-span. The equation of motion of the model having mass, damping and spring terms is expressed in the rotating coordinates as follows [9]:

$$m(\ddot{\xi} - 2\Omega\dot{\eta} - \Omega^2\xi) + c(\dot{\xi} - \Omega\eta) + k_{\xi}\xi + k_{\xi\eta}\eta = me\Omega^2 \cos\beta - mg\cos\Omega t,$$

$$m(\ddot{\eta} + 2\Omega\dot{\xi} - \Omega^2\eta) + c(\dot{\eta} + \Omega\xi) + k_{\eta\xi}\xi + k_{\eta}\eta = me\Omega^2 \sin\beta + mg\sin\Omega t.$$
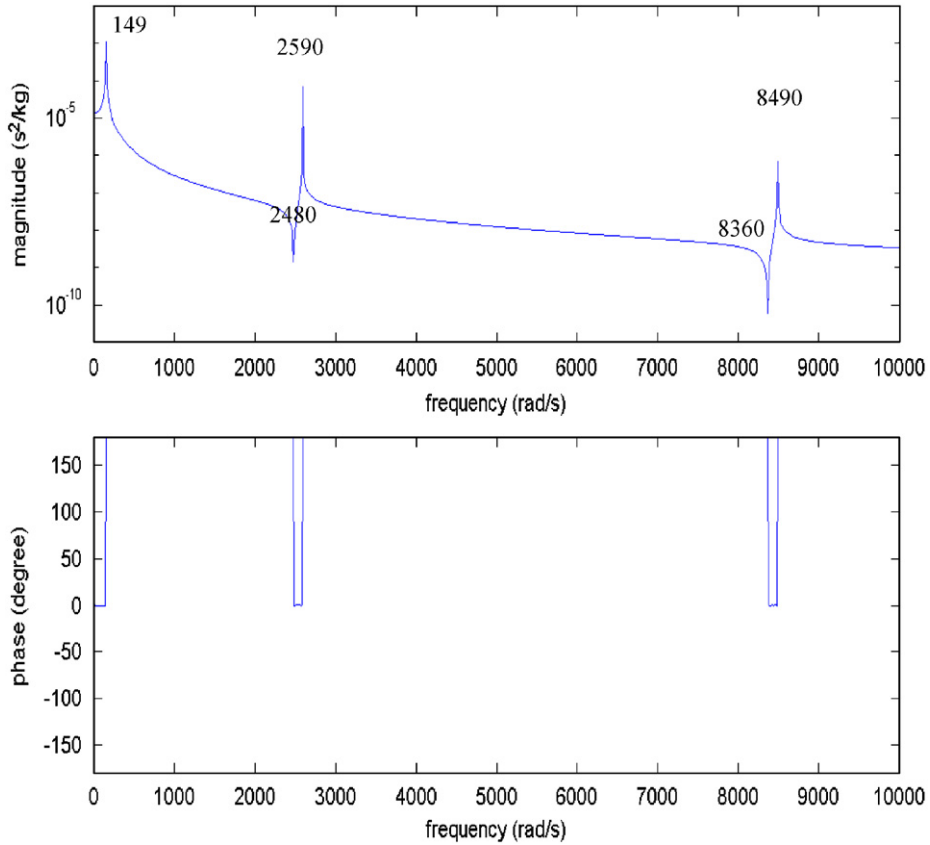
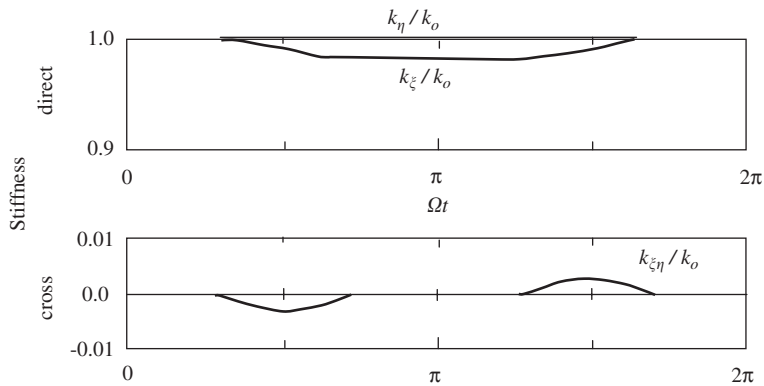Fig. 12. Influence coefficient between unbalance force at node 2 and displacement at node 3.

Fig. 13. Stiffness change with shaft rotation (without unbalance, crack depth $a/D = 0.2$) [9].

The simulation in Ref. [9] explained the crack breathing using the stiffness behavior. As the crack opens, the direct stiffness k_ξ and k_η decrease until the crack completely open as shown in Fig. 13, and they increase again to the uncracked rotor stiffness during closing. The cross-coupled stiffness, $k_{\xi\eta}(= k_{\eta\xi})$, is only non-zero when the crack is between the completely closed and completely open states.

In the current study crack breathing has been also considered. The additional slope at the crack is calculated by integrating on the open crack area, in a similar manner to that of Ref. [9]. The additional slope occurs only when the crack is open. Fig. 14 shows the change of the additional slope with shaft rotation. The additional

slope with respect to ξ axis, $\Delta\theta_\xi$, is partially related to the crack partial opening. To compare the simulations with the result of Ref. [9], a similar condition is considered. The horizontal axis of Fig. 14 indicates one revolution that the positive ξ axis crack direction experiences during a clockwise rotation from the positive horizontal direction as shown in Fig. 4. The crack remains closed for the region between 234° and 306°. The same result is shown in Fig. 13, where the horizontal axis indicates the rotation angle of the crack from the upward position. Zero on the horizontal axis in Fig. 14 is equivalent to $\pi/2$ in Fig. 13. The negative value in the additional slope is due to the adopted notations as explained in Section 3.1, indicating the crack opening. The harmonic components in the simulation are considered up to the fourth harmonics through this study.

As the crack propagates, both the duration of open crack status and the magnitude of additional slope increase. Comparison of the additional slope for different crack depths is shown in Fig. 15. The shaft rotates at very low speed of $\Omega = 1$ rad/s.

Monitoring the stress intensity factor on the crack front line during revolution, the crack behavior on the front line may be also explained. As the shaft rotates, the stress intensity factor on the crack front line begins to have positive value from the positive end point on η axis, and the point having the positive value propagates to the negative η direction along the crack front line. Each stress intensity factor would have repeated positive and negative values with a sine curve variation. The maximum stress in intensity factor values are different according to the position on the crack front line and crack depth. Also, it depends on the rotating speed even though it is not shown here. Fig. 16 shows the distribution of maximum value of stress intensity factor on the crack front line with the crack depth varied. Each crack front line is divided into 10 segments, and the center position of each segment is chosen to monitor the maximum stress intensity factor value. At shallow crack states, the central area of the crack front line has larger stress intensity factor values. As the crack depth increases, the dominant stress intensity factor region moves to both ends. After the crack passes the center of shaft, larger stress intensity factor values are located at both ends. This distribution of maximum stress intensity factor with the crack depth may be attributed to the crack propagation if we consider the beach mark test of Ref. [23]. According to test results, the crack propagation is dominant at the center in the initial state, and the dominant crack propagation region moves to the sides as the crack continues to propagate. Finally, the crack propagates dominantly at both ends of crack line after the crack line passes the shaft centerline.

The crack breathing is also affected by unbalance. The unbalance effect increases with the shaft rotation speed because the centrifugal force due to unbalance rapidly increases with speed. Fig. 17 shows the unbalance effect at $\Omega = 135$ rad/s which is below the first critical speed. The crack depth is 30%. If the unbalance is aligned with the crack, the crack opens easier. As shown in Fig. 17(b) the additional slope has a larger value than in the without unbalance case. When the unbalance is opposite to the crack, the centrifugal force induced by unbalance would reduce the crack opening and the additional slope as shown in Fig. 17(c). The unbalance
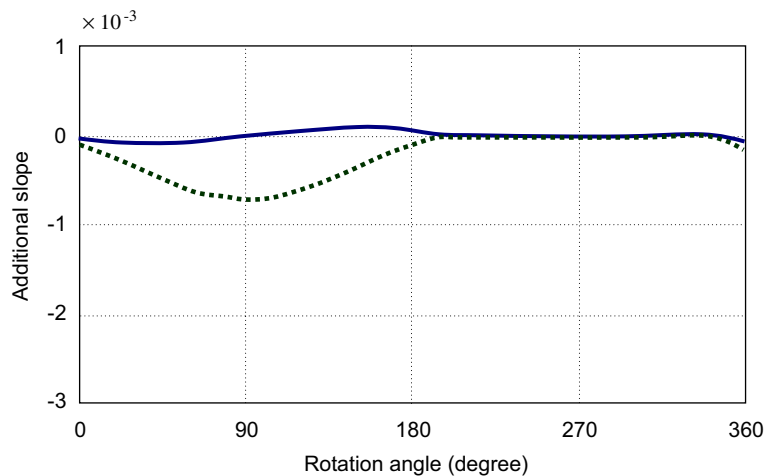

Fig. 14. Additional slope change with shaft rotation (without unbalance, $a/D = 0.2$, $\Omega = 74.5$ rad/s); solid line: $\Delta\theta_\xi$, dotted line: $\Delta\phi_\eta$.
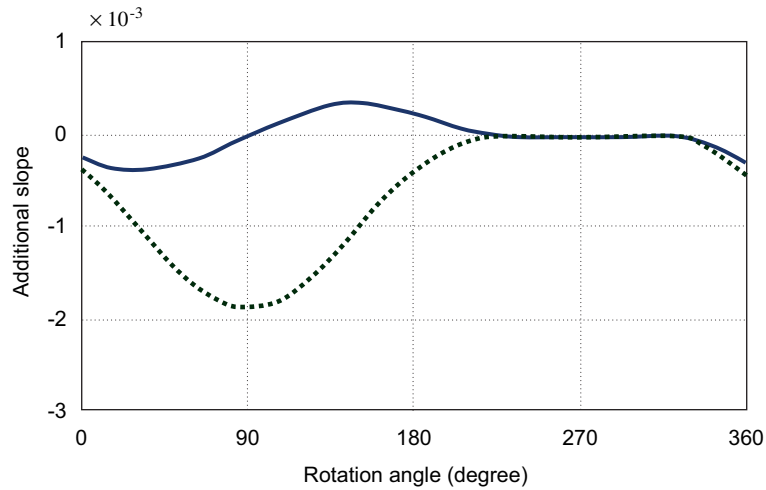
Fig. 15. Additional slope (without unbalance, $\Omega = 1$ rad/s); $a/D = 0.3$; solid line: $\Delta\theta_\xi$, dotted line: $\Delta\phi_\eta$.
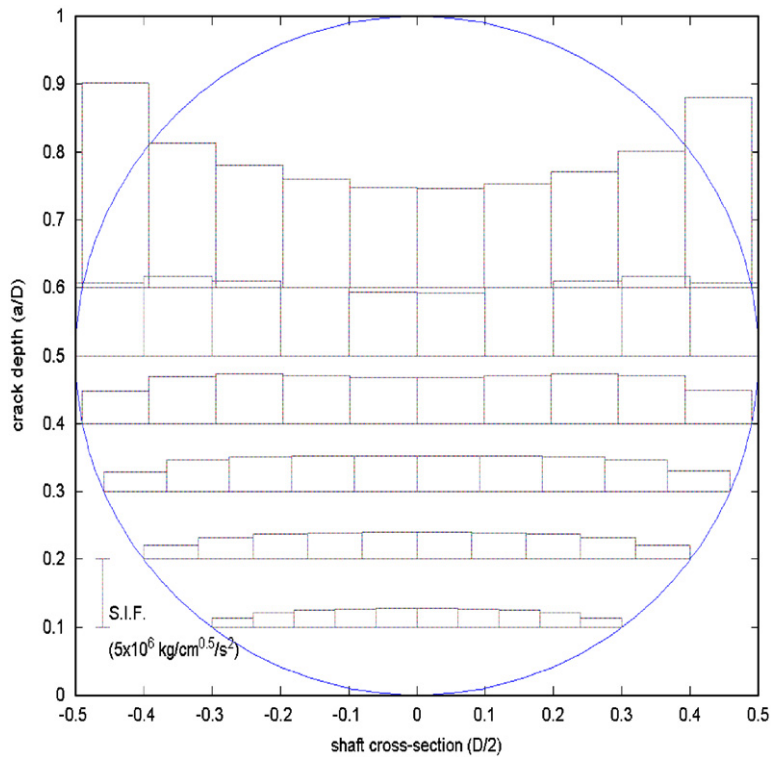

Fig. 16. Distribution of maximum stress intensity factor with crack depth increased (without unbalance, $\Omega = 100$ rad/s).

of 0.001 kg cm is applied at each disk. For each case shown in Fig. 17(a–c), the closed crack regions are 249°–291°, 250°–290° and 247°–293°, respectively.

Once the rotation speed passes over the critical speed, the unbalance effect on the response is reversed. Fig. 18 shows the response for a rotation speed $\Omega = 160$ rad/s which is above the critical speed. The response becomes out of phase with the input force. The centrifugal force due to unbalance will be directed towards the
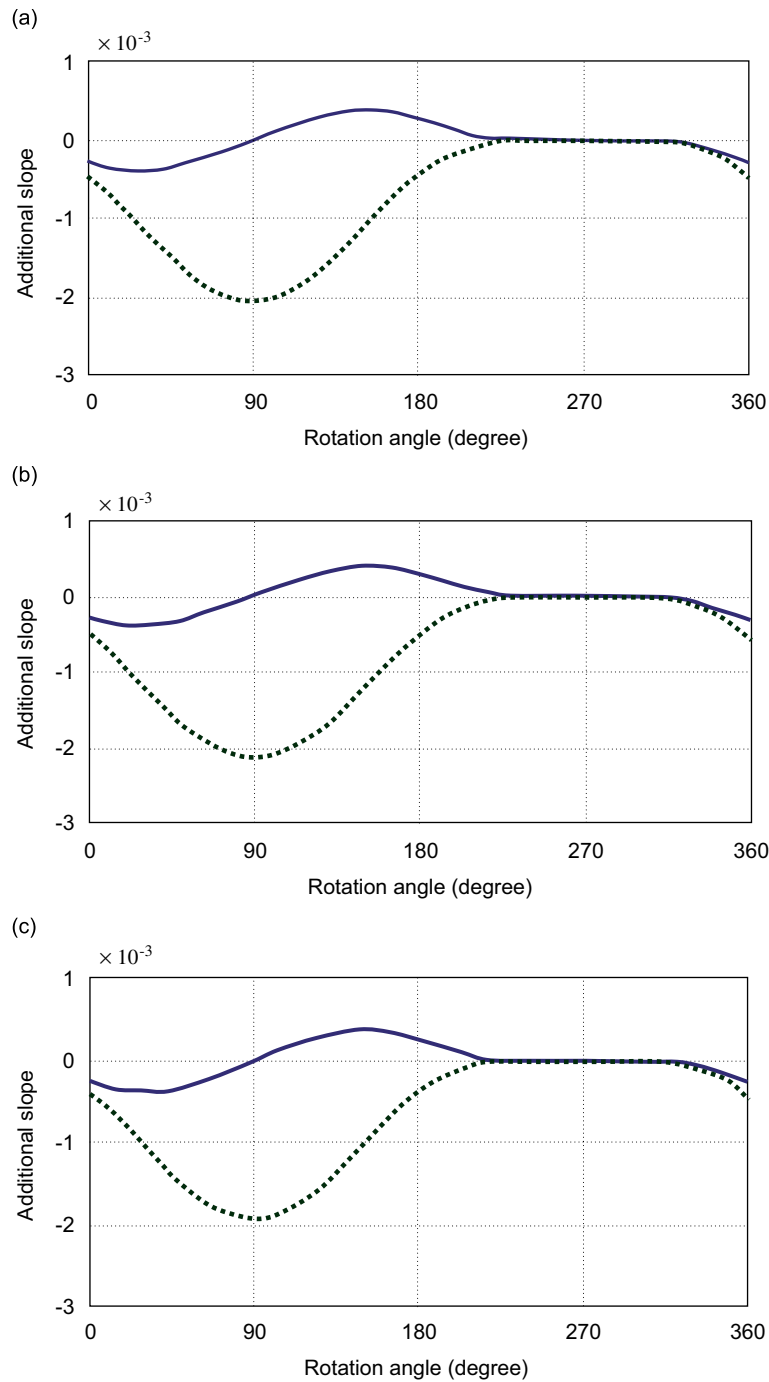
Fig. 17. Additional slope during one revolution ($a/D = 0.3$, $\Omega = 135$ rad/s): (a) without unbalance, (b) $m_2e_2 = m_4e_4 = 0.001$ kg cm, $\beta = 0°$ and (c) $m_2e_2 = m_4e_4 = 0.001$ kg cm, $\beta = 180°$.

rotation center line, thus an unbalance force aligned with the crack direction helps crack closure. If the unbalance is opposite to crack, i.e., $\beta = 180°$, it helps crack opening. Fig. 18 shows the results for this case.

The displacement of the shaft at the crack location of node 3 is analyzed to explain the dynamic motion. In view of the fact that the main objective of cracked rotor research is to extract ideas for diagnostics, it is
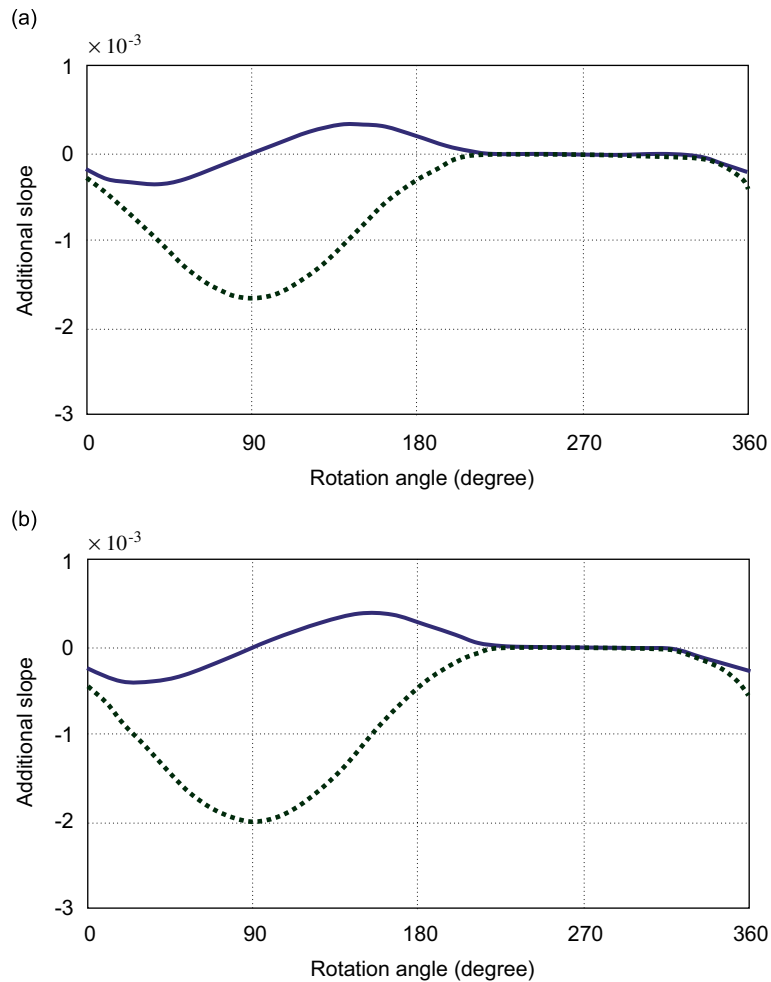
Fig. 18. Additional slope during one revolution ($a/D = 0.3$, $\Omega = 160\,\text{rad/s}$): (a) $m_2 e_2 = m_4 e_4 = 0.001\,\text{kg cm}$, $\beta = 0°$ and (b) $m_2 e_2 = m_4 e_4 = 0.001\,\text{kg cm}$, $\beta = 0°$.

important to discuss the shaft dynamic motion in detail. The static deflection at node 3 is 494 μm for the case without a crack. If there is no unbalance, the rotating shaft will stay at this static deflection level during crack closing, and will have more deflection during crack opening. The deflection shape would, therefore, take the form of a loop. However, the preceded statement should be modified when considering the transient effect of the dynamic motion during crack breathing. In this case, the shaft will no longer stay in the expected orbit during crack breathing. Fig. 19 shows orbits for the various speeds at an average speed much lower than the first critical speed when the crack depth is 10%. Because the shaft does not have an unbalance, which produces synchronous vibration, peculiar orbits having higher-harmonic components are observed in the region near to the sub-harmonic critical speeds. Figs. 20 and 21 show similar responses for the cases when the crack depth is increased to 20% and 30%, respectively. As expected, the vibration magnitude increases at a faster rate as the crack depth increases.

The dynamic behavior has been analyzed around the first critical speed range. Fig. 22 shows the orbits at the speed range from 136 to 151 rad/s for the case with no unbalance. The observation has been focused on the magnitude, whirl direction and phase of the orbit. The critical speed of the model is 149 rad/s without a crack as shown in Fig. 12. The orbit at 149 rad/s could not be obtained due to divergence. The orbit has a strong magnitude distribution near 138 rad/s and decreases with the increased speed, and then suddenly increases and decreases at 149 rad/s, which marks the critical speed of the normal model without a crack.
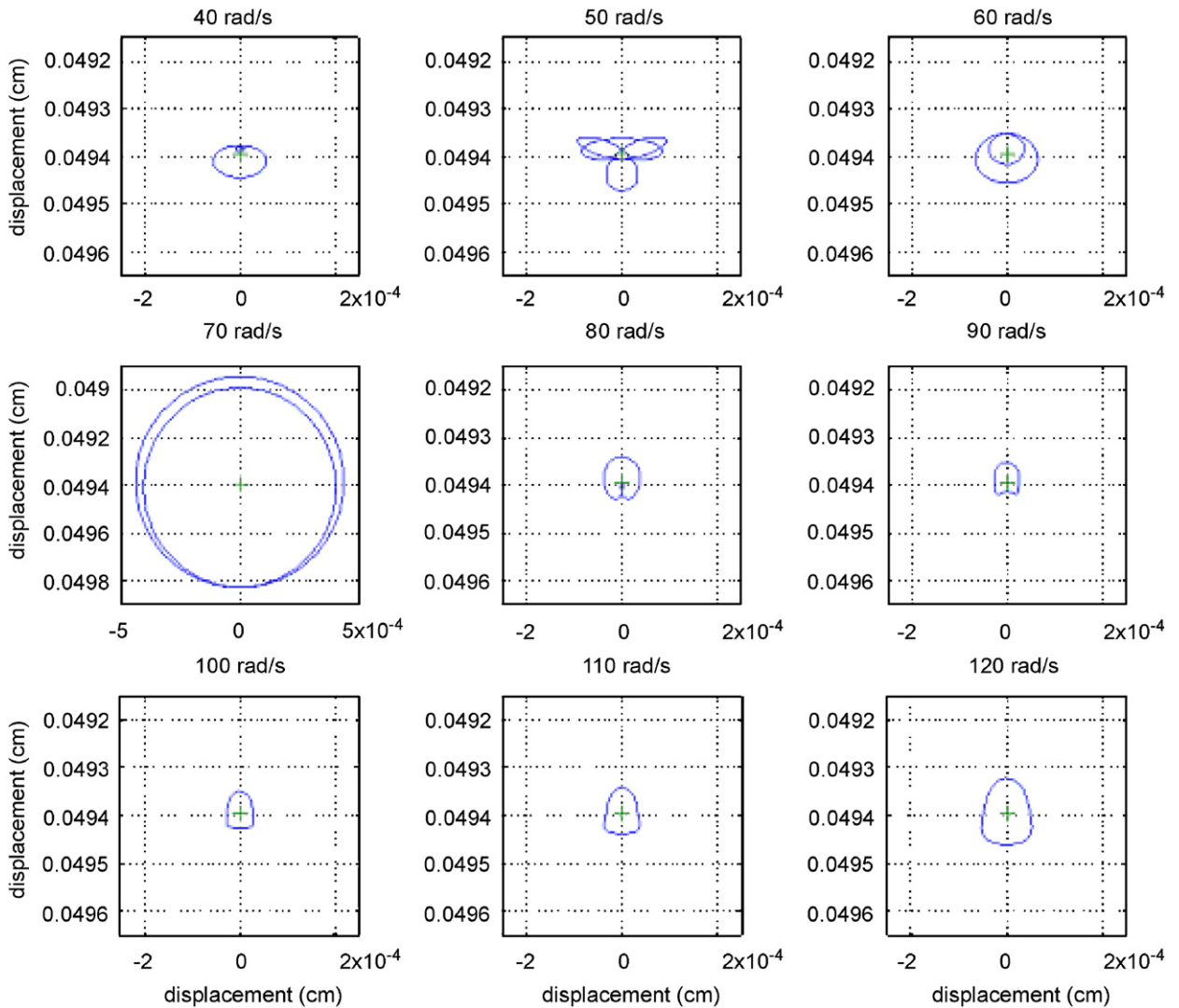
Fig. 19. Orbits as a function of rotation speed increases (without unbalance, $a/D = 0.1$).

The cross mark in the plots in Fig. 22 indicates the starting point of the orbit when $\Omega t = 0$. The whirl direction coincides with the shaft spin (clockwise) direction until 146 rad/s, and the whirl direction reverses to the counter-clockwise through the horizontally narrow elliptic orbit. The whirl direction reverses again through vertically narrow elliptic orbit. But the latter reversal takes much more wide speed range. Sekhar and Prabhu [24] stated the possibility that the backward whirl due to a crack exists. Another observation of the results shown in Fig. 22 relates to the phase shift. The orbit has the same phase with the crack direction until 138 rad/s. The orbit, then, becomes out of phase to the crack starting from a speed of 139 rad/s, and maintains this status until the speed reaches 149 rad/s.

The observations discussed above are based on simulation results using the model in this study. In practice, it is very difficult or rather impossible to fabricate a perfect cracked rotor without unbalance. This makes the experimental verification of the above simulation infeasible. It is well known that the critical speed decreases and the harmonics increase with an increase in crack depth. According to the above simulation results, there also exists some peculiar range near the critical speed, where the temporary whirl direction reversal and phase shift exist.
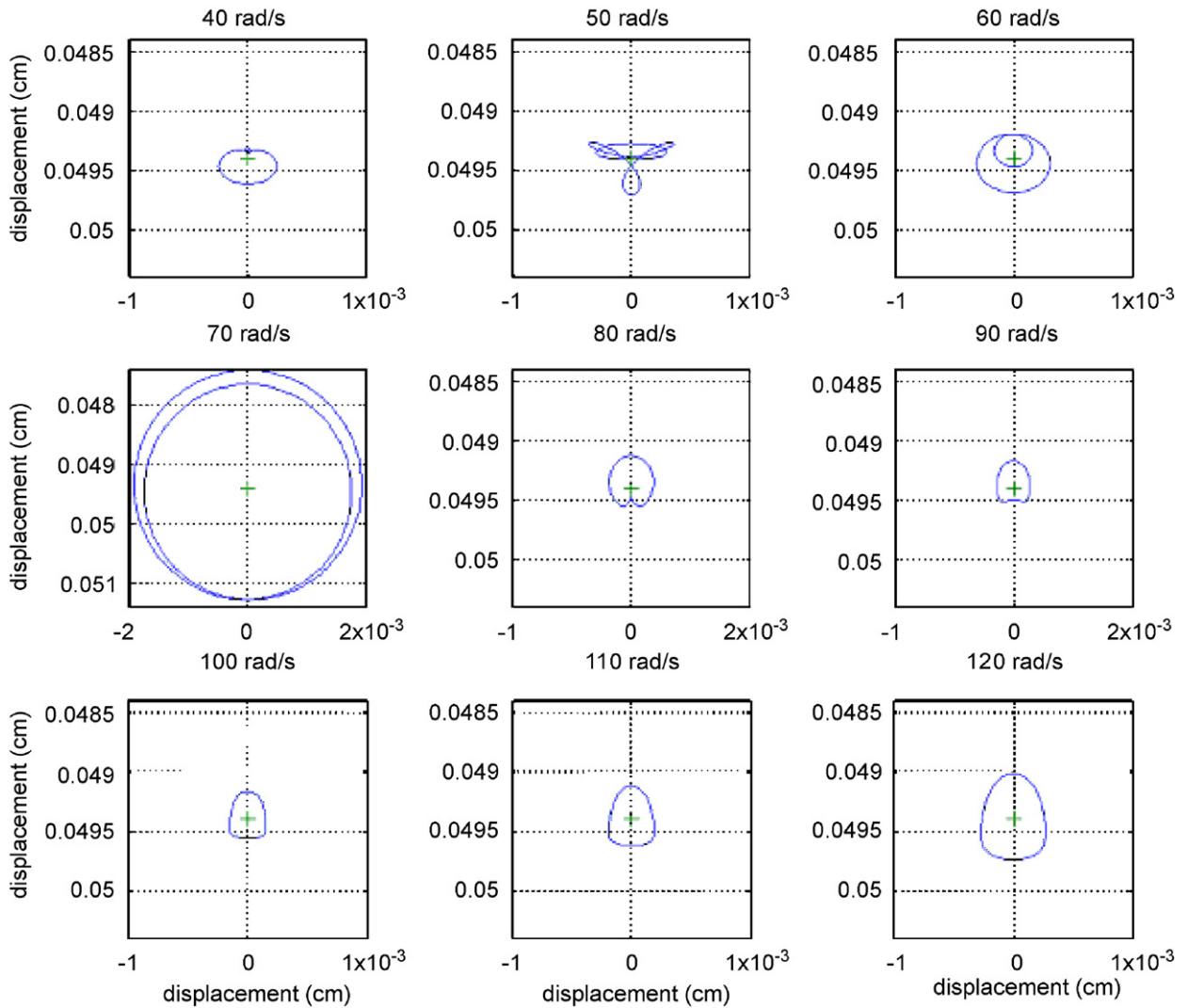
Fig. 20. Orbits as a function of rotation speed increased (without unbalance, $a/D = 0.2$).

If an unbalance is applied to the rotor, the motion becomes simpler. In Fig. 23 is shown the orbit when 0.001 kg cm unbalance is applied to each disk at nodes 2 and 4. The phase becomes out of phase when passing 149 rad/s, where the orbit diverges. The orbit has a large magnitude at 138 rad/s, but the magnitude is not much increased compared with the case without unbalance as shown in Fig. 22. Also, since the response is originally out of phase starting from 139 rad/s, the unbalance effect that produces the in phase response is small, especially at 139 rad/s, because the unbalance force which produces the in phase response is still smaller, the resultant response appears as out of phase. As the speed approaches the critical speed of the normal model without a crack, the orbit shows the typical unbalance response. Going back to Fig. 22 and comparing it with the response with unbalance, the large orbit near 138 rad/s seems be related to the particular stiffness asymmetry caused by the cracked rotor, which also gives rise to the phase shift.

7. Conclusions

The additional slope at the crack position is introduced as a self-excitation source of the cracked rotor vibration. Using a transfer matrix, the influence coefficients are analytically derived in order to calculate the
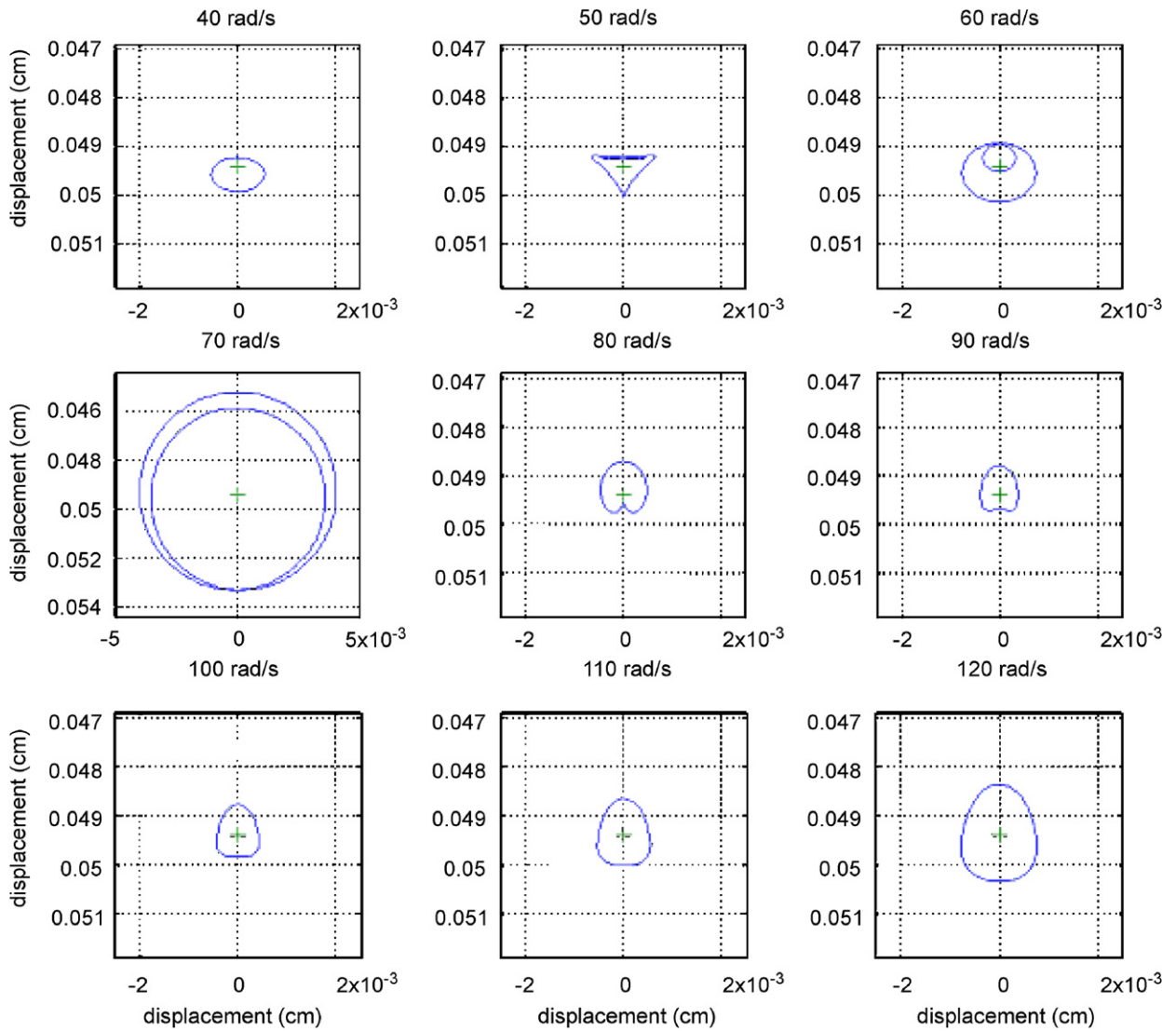
Fig. 21. Orbits as a function of rotation speed increased (without unbalance, $a/D = 0.3$).

dynamic response due to the unbalance and crack and the quasi-static response due to gravity. The additional slope is expressed as a function of the bending moment at the crack position based on a fracture mechanics concept, and inversely the bending moment is expressed as function of the additional slope at the crack position.

At each angle step during the shaft revolution, the additional slope and bending moment are calculated by using an iterative method. The additional slope is obtained by integrating over the crack region excluding the region where the stress intensity factor is negative because the compression state of stress indicates that the crack is closed, and thus would not contribute to the additional deflection. Also, the bending moment at crack position is calculated using the additional slope as one of the input data. Because the crack breathing produces a nonlinear excitation to the system, the transient behavior is considered by introducing a 'moving' Fourier-series expansion concept for the additional slope. The time-varying harmonic components of the additional slope are used to produce the harmonic responses.

The application considered is for a general rotor model consisting of multiple shafts, disks and cracks, and resilient bearings at both ends. Also, simulations are carried out for a simple rotor, similar to those described in the literature, and a comparison of the basic crack behavior is shown.
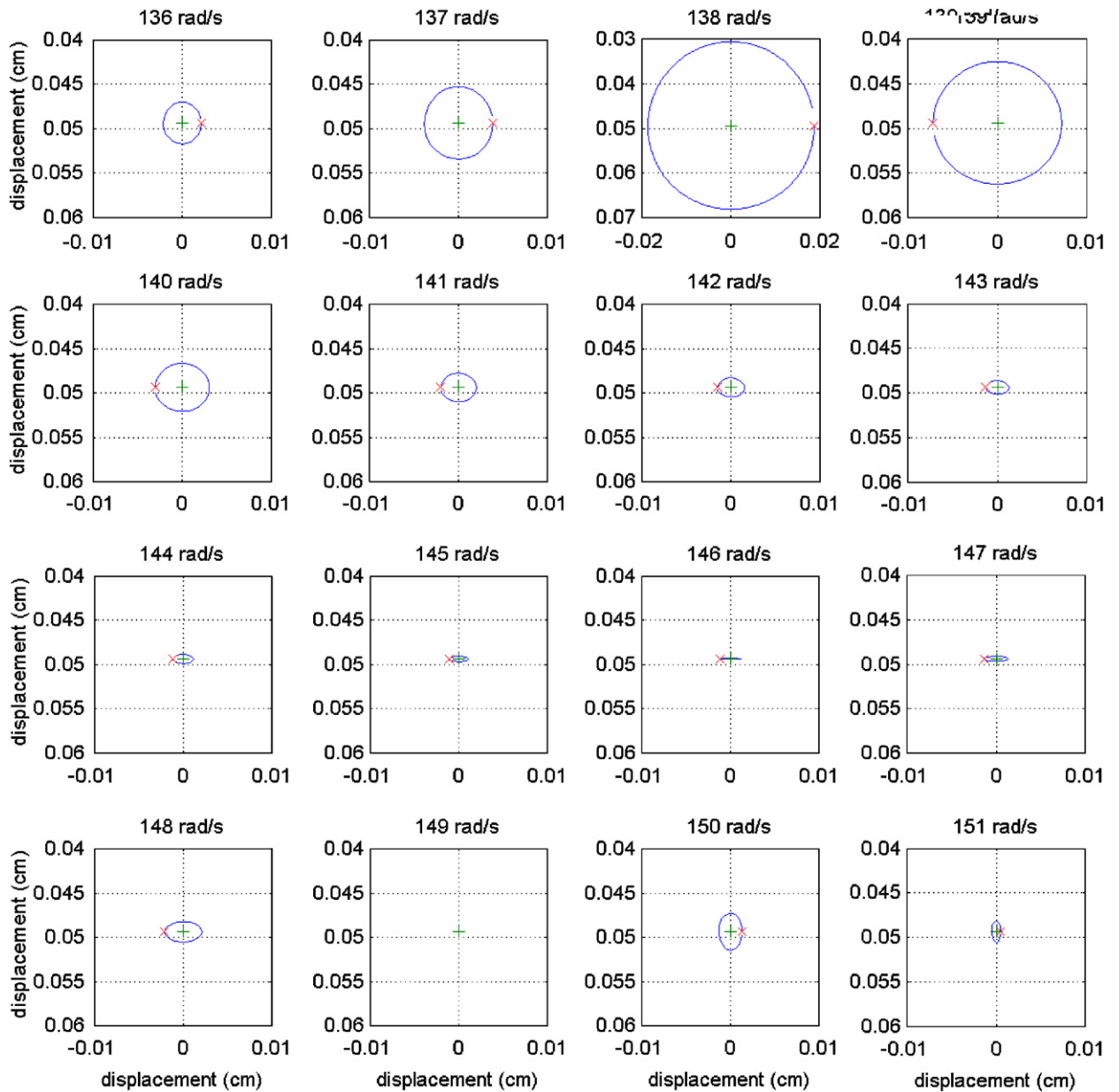
Fig. 22. Orbits as a function of rotation speed increased (without unbalance, $a/D = 0.2$).

Using the additional slope, the cracked rotor behavior is explained with the crack depth and rotation speed increased: the magnitude of the additional slope increases and the closed crack duration during a revolution decreases as the crack depth increases. The maximum value of stress intensity factor is different along the crack front line, crack depth and rotating speed. At shallow crack states, the central area of the crack front line has larger stress intensity factor value. As the crack depth increases, the dominant stress intensity factor value region moves to both ends, and finally the larger stress intensity factor values exist at both ends after the crack passes the centerline of shaft. The result matches the crack propagation pattern shown in the bench mark tests described in the literature very well.
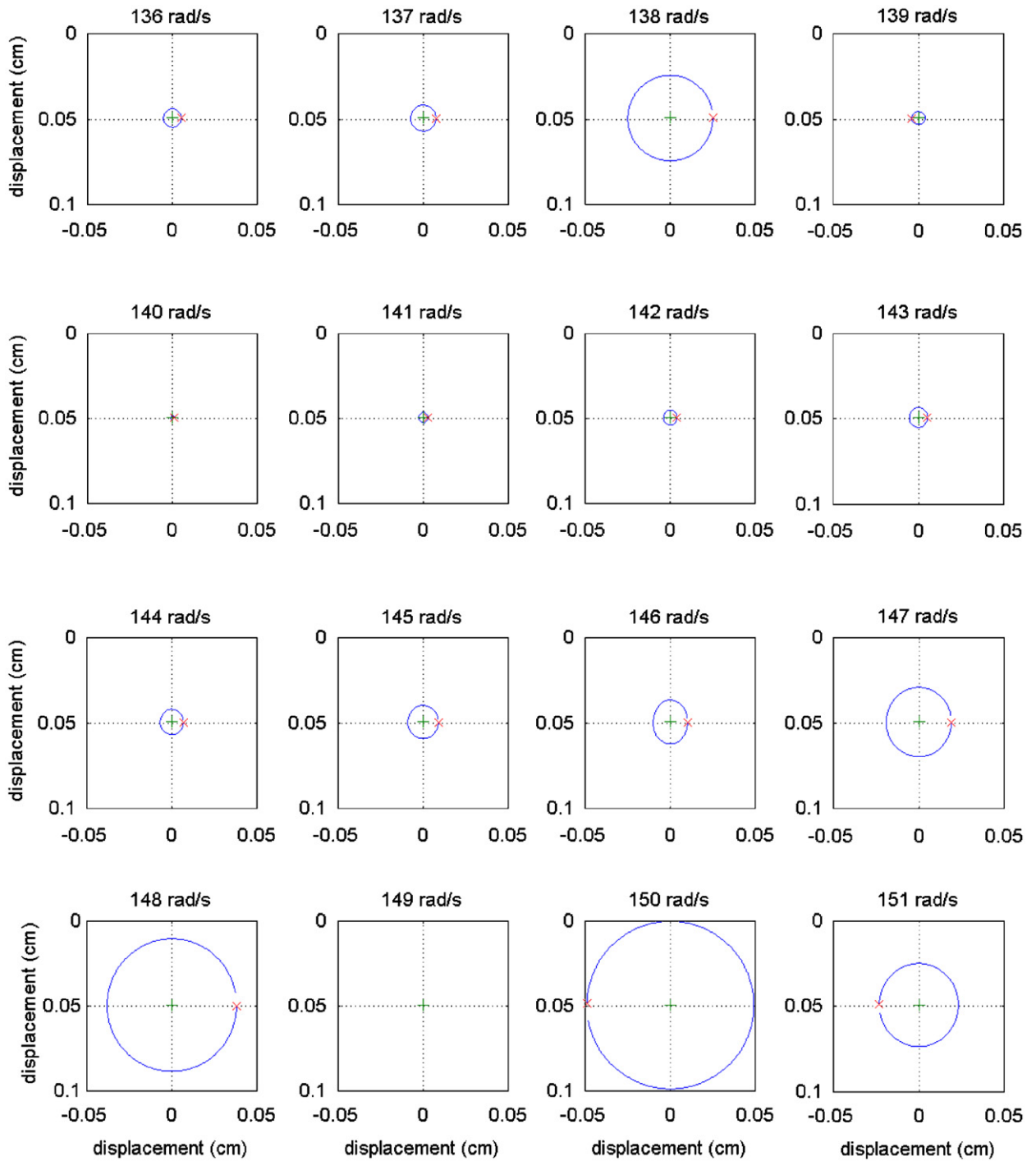
Fig. 23. Orbits as a function of rotation speed increased ($m_2e_2 = m_4e_4 = 0.001\,\mathrm{kg\,cm}$, $a/D = 0.2$).

Whirl orbits are discussed near the critical and sub-critical speed ranges. Based on the simulation results, there exists some unstable range near the critical speed, where the temporary whirl direction reversal and phase shift exist. The phenomenon seems to be due to the nonlinear stiffness asymmetry.

When an unbalance is applied, features such as the whirl direction reversal and phase shaft disappear.

Appendix A. State vector and transfer matrix for dynamic response [20]

A.1. For shaft element

The equation of motion of the rotating shaft is written as follows [21]:

$$
\begin{aligned}
EI\frac{\partial^4 u}{\partial x^4} - \frac{EI\rho}{\kappa G}\frac{\partial^4 u}{\partial x^2 \partial t^2} - jT\frac{\partial^3 u}{\partial x^3} + j\frac{T\rho}{\kappa G}\frac{\partial^3 u}{\partial x \partial t^2} + \rho A\frac{\partial^2 u}{\partial t^2} \\
- \rho A r_o^2 \left[\left(\frac{\partial^4 u}{\partial x^2 \partial t^2} -\right)\right] - j2\Omega\left(-\frac{\rho}{\kappa G}\frac{\partial^3 u}{\partial x^2 \partial t}\right) = 0.
\end{aligned}
\tag{A.1}
$$

The harmonic motion of natural frequency ω can be separated in the variable $u(x, t)$ of Eq. (A.1) as

$$
u(x, t) = U(x)\mathrm{e}^{j\omega t}.
\tag{A.2}
$$

Substituting Eq. (A.2) into Eq. (A.1) results in the following equation:

$$
\frac{\mathrm{d}^4 U}{\mathrm{d}x^4} + a\frac{\mathrm{d}^3 U}{\mathrm{d}x^3} + b\frac{\mathrm{d}^2 U}{\mathrm{d}x^2} + c\frac{\mathrm{d}U}{\mathrm{d}x} + \mathrm{d}\, U = 0,
\tag{A.3}
$$

where

$$
\begin{aligned}
a &= -\frac{jT}{EI}, \\
b &= \frac{1}{EI}\left[\left(\frac{EI\rho}{\kappa G} + \rho A r_0^2\right)\omega^2 - 2\rho A r_0^2 \Omega\omega\right], \\
c &= -j\frac{1}{EI}\frac{T\rho}{\kappa G}\omega^2, \\
d &= \frac{1}{EI}\left[\frac{\rho^2 A r_0^2}{\kappa G}\omega^4 - 2\frac{\rho^2 A r_0^2 \Omega}{\kappa G}\omega^3 - \rho A\omega^2\right].
\end{aligned}
\tag{A.4}
$$

Using the four roots of the polynomial [25,26], the solution of Eq. (A.4) is expressed as

$$
U = p_1 e^{\lambda_1 x} + p_2 e^{\lambda_2 x} + p_3 e^{\lambda_3 x} + p_4 e^{\lambda_4 x}.
\tag{A.5}
$$

Eq. (A.5) means that the elastodynamic behavior of the rotating shaft is dependent on λ's, which are determined by several parameters, such as rotating speed Ω, natural frequency ω, and geometric and material properties of the shaft. The coefficients p_1, p_2, p_3, p_4, of Eq. (A.5) are also complex values defined in a uniform shaft segment [26].

The state variables at $x = 0$, i.e. at the left-hand side of shaft element, are expressed from Eq. (2) and (A.5) as follows:

$$
\begin{aligned}
U_0 &= p_1 + p_2 + p_3 + p_4, \\
\alpha_0 &= \lambda_1 p_1 + \lambda_2 p_2 + \lambda_3 p_3 + \lambda_4 p_4, \\
M_0 &= g_1 p_1 + g_2 p_2 + g_3 p_3 + g_4 p_4, \\
V_0 &= h_1 p_1 + h_2 p_2 + h_3 p_3 + h_4 p_4,
\end{aligned}
\tag{A.6}
$$

where

$$
\begin{aligned}
&g_1 = EI\lambda_1^2 - jT\lambda_1, \; g_2 = EI\lambda_2^2 - jT\lambda_2, \\
&g_3 = EI\lambda_3^2 - jT\lambda_3, \; g_4 = EI\lambda_4^2 - jT\lambda_4, \\
&h_1 = EI\lambda_1^3 + \rho A r_o^2(\omega^2 - 2\omega\Omega)\lambda_1 - jT\lambda_1^2, \\
&h_2 = EI\lambda_2^3 + \rho A r_o^2(\omega^2 - 2\omega\Omega)\lambda_2 - jT\lambda_2^2, \\
&h_3 = EI\lambda_3^3 + \rho A r_o^2(\omega^2 - 2\omega\Omega)\lambda_3 - jT\lambda_3^2, \\
&h_4 = EI\lambda_4^3 + \rho A r_o^2(\omega^2 - 2\omega\Omega)\lambda_4 - jT\lambda_4^2.
\end{aligned}
\tag{A.7}
$$

Expressing the coefficients p_1, p_2, p_3, p_4 in terms of U_0, α_0, M_0, V_0, from Eq. (A.6) and substituting them into the expressions of U_1, α_1, M_1, V_1, at $x = l$, the relation between the state vectors on each side of a shaft element having length l is written as follows:

$$
\begin{pmatrix} U_l \\ \alpha_l \\ M_l \\ V_l \end{pmatrix}
= \frac{1}{\Delta}
\begin{bmatrix}
a_{11} & a_{12} & a_{13} & a_{14} \\
a_{21} & a_{22} & a_{23} & a_{24} \\
a_{31} & a_{32} & a_{33} & a_{34} \\
a_{41} & a_{42} & a_{43} & a_{44}
\end{bmatrix}
\begin{pmatrix} U_0 \\ \alpha_0 \\ M_0 \\ V_0 \end{pmatrix},
\tag{A.8}
$$

where

$$
\Delta = \begin{vmatrix}
1 & 1 & 1 & 1 \\
\lambda_1 & \lambda_2 & \lambda_3 & \lambda_4 \\
g_1 & g_2 & g_3 & g_4 \\
h_1 & h_2 & h_3 & h_4
\end{vmatrix}, \;
a_{11} = \begin{vmatrix}
e^{\lambda_1 l} & e^{\lambda_2 l} & e^{\lambda_3 l} & e^{\lambda_4 l} \\
\lambda_1 & \lambda_2 & \lambda_3 & \lambda_4 \\
g_1 & g_2 & g_3 & g_4 \\
h_1 & h_2 & h_3 & h_4
\end{vmatrix},
$$

$$
a_{12} = \begin{vmatrix}
1 & 1 & 1 & 1 \\
e^{\lambda_1 l} & e^{\lambda_2 l} & e^{\lambda_3 l} & e^{\lambda_4 l} \\
g_1 & g_2 & g_3 & g_4 \\
h_1 & h_2 & h_3 & h_4
\end{vmatrix}, \;
a_{13} = \begin{vmatrix}
1 & 1 & 1 & 1 \\
\lambda_1 & \lambda_2 & \lambda_3 & \lambda_4 \\
e^{\lambda_1 l} & e^{\lambda_2 l} & e^{\lambda_3 l} & e^{\lambda_4 l} \\
h_1 & h_2 & h_3 & h_4
\end{vmatrix},
$$

$$
a_{14} = \begin{vmatrix}
1 & 1 & 1 & 1 \\
\lambda_1 & \lambda_2 & \lambda_3 & \lambda_4 \\
g_1 & g_2 & g_3 & g_4 \\
e^{\lambda_1 l} & e^{\lambda_2 l} & e^{\lambda_3 l} & e^{\lambda_4 l}
\end{vmatrix}, \;
a_{21} = \begin{vmatrix}
\lambda_1 e^{\lambda_1 l} & \lambda_2 e^{\lambda_2 l} & \lambda_3 e^{\lambda_3 l} & \lambda_4 e^{\lambda_4 l} \\
\lambda_1 & \lambda_2 & \lambda_3 & \lambda_4 \\
g_1 & g_2 & g_3 & g_4 \\
h_1 & h_2 & h_3 & h_4
\end{vmatrix},
$$

$$
a_{22} = \begin{vmatrix}
1 & 1 & 1 & 1 \\
\lambda_1 e^{\lambda_1 l} & \lambda_2 e^{\lambda_2 l} & \lambda_3 e^{\lambda_3 l} & \lambda_4 e^{\lambda_4 l} \\
g_1 & g_2 & g_3 & g_4 \\
h_1 & h_2 & h_3 & h_4
\end{vmatrix}, \;
a_{23} = \begin{vmatrix}
1 & 1 & 1 & 1 \\
\lambda_1 & \lambda_2 & \lambda_3 & \lambda_4 \\
\lambda_1 e^{\lambda_1 l} & \lambda_2 e^{\lambda_2 l} & \lambda_3 e^{\lambda_3 l} & \lambda_4 e^{\lambda_4 l} \\
h_1 & h_2 & h_3 & h_4
\end{vmatrix},
$$

$$
a_{24} = \begin{vmatrix}
1 & 1 & 1 & 1 \\
\lambda_1 & \lambda_2 & \lambda_3 & \lambda_4 \\
g_1 & g_2 & g_3 & g_4 \\
\lambda_1 e^{\lambda_1 l} & \lambda_2 e^{\lambda_2 l} & \lambda_3 e^{\lambda_3 l} & \lambda_4 e^{\lambda_4 l}
\end{vmatrix}, \;
a_{31} = \begin{vmatrix}
g_1 e^{\lambda_1 l} & g_2 e^{\lambda_2 l} & g_3 e^{\lambda_3 l} & g_4 e^{\lambda_4 l} \\
\lambda_1 & \lambda_2 & \lambda_3 & \lambda_4 \\
g_1 & g_2 & g_3 & g_4 \\
h_1 & h_2 & h_3 & h_4
\end{vmatrix},
$$

$$a_{32} = \begin{vmatrix} 1 & 1 & 1 & 1 \\ g_1 e^{\lambda_1 l} & g_2 e^{\lambda_2 l} & g_3 e^{\lambda_3 l} & g_4 e^{\lambda_4 l} \\ g_1 & g_2 & g_3 & g_4 \\ h_1 & h_2 & h_3 & h_4 \end{vmatrix}, \quad a_{33} = \begin{vmatrix} 1 & 1 & 1 & 1 \\ \lambda_1 & \lambda_2 & \lambda_3 & \lambda_4 \\ g_1 e^{\lambda_1 l} & g_2 e^{\lambda_2 l} & g_3 e^{\lambda_3 l} & g_4 e^{\lambda_4 l} \\ h_1 & h_2 & h_3 & h_4 \end{vmatrix},$$

$$a_{34} = \begin{vmatrix} 1 & 1 & 1 & 1 \\ \lambda_1 & \lambda_2 & \lambda_3 & \lambda_4 \\ g_1 & g_2 & g_3 & g_4 \\ g_1 e^{\lambda_1 l} & g_2 e^{\lambda_2 l} & g_3 e^{\lambda_3 l} & g_4 e^{\lambda_4 l} \end{vmatrix}, \quad a_{41} = \begin{vmatrix} h_1 e^{\lambda_1 l} & h_2 e^{\lambda_2 l} & h_3 e^{\lambda_3 l} & h_4 e^{\lambda_4 l} \\ \lambda_1 & \lambda_2 & \lambda_3 & \lambda_4 \\ g_1 & g_2 & g_3 & g_4 \\ h_1 & h_2 & h_3 & h_4 \end{vmatrix},$$

$$a_{42} = \begin{vmatrix} 1 & 1 & 1 & 1 \\ h_1 e^{\lambda_1 l} & h_2 e^{\lambda_2 l} & h_3 e^{\lambda_3 l} & h_4 e^{\lambda_4 l} \\ g_1 & g_2 & g_3 & g_4 \\ h_1 & h_2 & h_3 & h_4 \end{vmatrix}, \quad a_{43} = \begin{vmatrix} 1 & 1 & 1 & 1 \\ \lambda_1 & \lambda_2 & \lambda_3 & \lambda_4 \\ h_1 e^{\lambda_1 l} & h_2 e^{\lambda_2 l} & h_3 e^{\lambda_3 l} & h_4 e^{\lambda_4 l} \\ h_1 & h_2 & h_3 & h_4 \end{vmatrix},$$

$$a_{44} = \begin{vmatrix} 1 & 1 & 1 & 1 \\ \lambda_1 & \lambda_2 & \lambda_3 & \lambda_4 \\ g_1 & g_2 & g_3 & g_4 \\ h_1 e^{\lambda_1 l} & h_2 e^{\lambda_2 l} & h_3 e^{\lambda_3 l} & h_4 e^{\lambda_4 l} \end{vmatrix}.$$

Eq. (A.8) is rewritten using the vectors and matrix in a simple form

$$\{s\}_{i+1}^L = [F]_i \{s\}_i^R, \tag{A.9}$$

where $[F]_i$ is the transfer matrix of the ith shaft element. $\{s\}$ is the complex state vector, subscript i of the state vector is the node number, and superscript L and R denote the left- and right-hand sides of the node, respectively. The state vectors are shown below in detail:

$$\{s\}_{i+1}^L = \begin{pmatrix} U_{i+1} \\ \alpha_{i+1} \\ M_{i+1} \\ V_{i+1} \end{pmatrix}^L, \quad \{s\}_i^R = \begin{pmatrix} U_i \\ \alpha_i \\ M_i \\ V_i \end{pmatrix}^R. \tag{A.10}$$

A.2. For disk element

$$\begin{pmatrix} U_i \\ \alpha_i \\ M_i \\ V_i \end{pmatrix}^R = \begin{bmatrix} 1 & 0 & 0 & 0 \\ 0 & 1 & 0 & 0 \\ 0 & (\omega \Omega J_p - \omega^2 J_t) & 1 & 0 \\ m_j \omega^2 - jc\omega & 0 & 0 & 1 \end{bmatrix} \begin{pmatrix} U_i \\ \alpha_i \\ M_i \\ V_i \end{pmatrix}^L + \begin{Bmatrix} 0 \\ 0 \\ 0 \\ m_i e_i \Omega^2 e^{j(\Omega t + \beta_i)} \end{Bmatrix} \tag{A.11}$$

or $\{s\}_i^R = [S]_i \{s\}_i^L + \{u\}_i$

A.3. For resilient springs

The bearings in this study are assumed to have the equivalent, direct components, $k_{YY} = k_{ZZ}$, only ($k_{YZ} = k_{ZY} = 0$).

For the resilient support at left end:

$$V_1^R = -kU_1^L \quad \text{where} \quad U_1^L = U_1^R. \tag{A.12}$$

For the resilient support at right end:

$$0 = V_N^L - kU_N^L \quad \text{where} \quad U_N^L = U_N^R. \tag{A.13}$$

Appendix B. State vector and transfer matrix for static gravity response

B.1. For shaft element

Since the gravity response is independent of time, the equation of motion (12) becomes an ordinary differential equation of the time-independent variable U_g as follows:

$$EI\frac{\mathrm{d}^4 U_g}{\mathrm{d}x^4} - jT\frac{\mathrm{d}^3 U_g}{\mathrm{d}x^3} = j\rho Ag. \tag{B.1}$$

For simplicity, ignoring the torque applied at both ends, the gravity response curve is given by

$$U_g = j\frac{\rho Ag}{24EI}x^4 + c_3 x^3 + c_2 x^2 + c_1 x + c_0. \tag{B.2}$$

The constants c_i are determined by boundary conditions.

By the similar method used for the dynamic response the relation between state vectors of each side of shaft element due to gravity

$$\begin{pmatrix} U_g \\ \alpha_g \\ M_g \\ V_g \end{pmatrix}^R = \begin{bmatrix} 1 & l & \dfrac{l^2}{2EI} & \dfrac{l^3}{6EI} \\ 0 & 1 & \dfrac{l}{EI} & \dfrac{l^2}{2EI} \\ 0 & 0 & 1 & l \\ 0 & 0 & 0 & 1 \end{bmatrix} \begin{pmatrix} U_g \\ \alpha_g \\ M_g \\ V_g \end{pmatrix}^L + \begin{pmatrix} \dfrac{\rho Agl^4}{24EI} \\ \dfrac{\rho Agl^3}{6EI} \\ \dfrac{\rho Agl^2}{2} \\ \rho Agl \end{pmatrix} e^{j(\pi/2)}, \tag{B.3}$$

where l is the length of the shaft element.

The above equation is rewritten as follows:

$$\{s_g\}^R = [F_g]\{s_g\}^L + \{g\}e^{j(\pi/2)}. \tag{B.4}$$

Since the state vector is expressed on the node through this paper, the above equation is rewritten as

$$\{s_g\}_{i+1}^L = [F_g]_i\{s_g\}_i^R + \{g\}_i e^{j(\pi/2)}, \tag{B.5}$$

where the subscript i in $[F_g]_i$ and $\{g\}i$ indicates the number of the shaft element.

B.2. For disk element

The relation between state vectors of each side of a disk due to gravity is written as follows:

$$\begin{pmatrix} U_g \\ \alpha_g \\ M_g \\ V_g \end{pmatrix}^R = \begin{bmatrix} 1 & 0 & 0 & 0 \\ 0 & 1 & 0 & 0 \\ 0 & 0 & 1 & 0 \\ 0 & 0 & 0 & 1 \end{bmatrix} \begin{pmatrix} U_g \\ \alpha_g \\ M_g \\ V_g \end{pmatrix}^L + \begin{pmatrix} 0 \\ 0 \\ 0 \\ mg \end{pmatrix} e^{j(\pi/2)} \tag{B.6}$$

or

$$\{s_g\}_i^R = \{s_g\}_i^L + \{d_g\}_i e^{j(\pi/2)}, \tag{B.7}$$

where m is the mass of disk.

B.3. For resilient springs

The bearings in this study are assumed to have the equivalent, direct components, $k_{YY} = k_{ZZ}$, only ($k_{YZ} = k_{ZY} = 0$).

For the resilient support at left end:

$$V_{g,1}^R = -kU_{g,1}^L \quad \text{where} \quad U_{g,1}^L = U_{g,1}^R. \tag{B.8}$$

For the resilient support at right end:

$$0 = V_{g,N}^L - kU_{g,N}^L \quad \text{where} \quad U_{g,N}^L = U_{g,N}^R. \tag{B.9}$$

References

[1] A.D. Dimarogonas, S.A. Paipetis, *Analytical Methods in Rotor Dynamics*, Applied Science Publishers Ltd., London, 1983 (Chapter 6).

[2] A.D. Dimarogonas, C.A. Papadopoulos, Vibration of cracked shafts in bending, *Journal of Sound and Vibration* 91 (1983) 583–593.

[3] A.D. Dimarogonas, Vibration of cracked structures: a state of the art review, *Engineering Fracture Mechanics* 55 (1996) 831–857.

[4] J. Wauer, On the dynamics of cracked rotors: a literature survey, *Applied Mechanics Reviews—Transactions of the ASME* 43 (1990) 13–17.

[5] R. Gasch, Dynamic behaviour of a simple rotor with a cross-sectional crack, *Vibration in Rotating Machinery*, Institution of Mechanical Engineers, London, 1976, pp. 123–128.

[6] G.B. Thomas, The application of non-linear methods to turbo-generator rotordynamics, *Vibration in Rotating Machinery*, Institution of Mechanical Engineers, London, 1979, pp. 209–216.

[7] I.W. Mayes, W.G.R. Davies, A method of calculating the vibrational behaviour of coupled rotating shafts containing a transverse crack, *Vibration in Rotating Machinery*, Institution of Mechanical Engineers, London, 1980, pp. 17–27.

[8] I.W. Mayes, W.G.R. Davies, Analysis of the response of a multi-rotor-bearing system containing a transverse crack in a rotor, *Journal of Vibration, Stress, and Reliability in Design—Transactions of the ASME* 106 (1984) 139–145.

[9] O.S. Jun, H.J. Eun, Y.Y. Earmme, C.-W. Lee, Modelling and vibration analysis of a simple rotor with a breathing crack, *Journal of Sound and Vibration* 155 (1992) 273–290.

[10] H. Tada, P.C. Paris, G.R. Irwin, *The Stress Analysis of Cracks Handbook*, third ed., ASME Press, New York, 2000.

[11] A.K. Darpe, K. Gupta, A. Chawla, Analysis of the response of a cracked Jeffcott rotor to axial excitation, *Journal of Sound and Vibration* 249 (2002) 429–445.

[12] A.K. Darpe, K. Gupta, A. Chawla, Transient response and breathing behaviour of a cracked Jeffcott rotor, *Journal of Sound and Vibration* 272 (2004) 207–243.

[13] H.D. Nelson, C. Nataraj, The dynamics of a rotor system with a cracked shaft, *Journal of Vibration, Acoustics, Stress, and Reliability in Design—Transactions of the ASME* 108 (1986) 189–196.

[14] H. Keiner, M.S. Gadala, Comparison of different modeling techniques to simulate the vibration of a cracked rotor, *Journal of Sound and Vibration* 254 (2002) 1012–1024.

[15] M.A. Prohl, A general method for calculating critical speeds of flexible rotors, *Journal of Applied Mechanics—Transactions of the ASME* 67 (1945) A-142–A-148.

[16] J.W. Lund, Stability and damped critical speeds of a flexible rotor in fluid-film bearings, *Journal for Engineering for Industry—Transactions of the ASME* (1974) 509–517.

[17] J.S. Rao, *Rotor Dynamics*, third ed., New Age International Ltd., 1996 (Chapter 8).

[18] T.C. Tsai, Y.Z. Wang, Vibration analysis and diagnosis of a cracked shaft, *Journal of Sound and Vibration* 192 (1996) 607–620.

[19] T.C. Tsai, Y.Z. Wang, The vibration of a multi-crack rotor, *International Journal of Mechanical Sciences* 39 (1997) 1037–1053.

[20] O.S. Jun, Influence coefficients on rotor having thick shaft elements and resilient bearings, *Journal of Sound and Vibration* 272 (2004) 657–673.

[21] C.-W. Lee, *Vibration Analysis of Rotors*, Kluwer Academic Publishers, The Netherlands, 1993 (Chapter 8).

[22] O.S. Jun, Dynamic Behavior of a Rotating Shaft Containing a Breathing Crack, PhD Dissertation, Korea Advanced Institute of Science and Technology, 1991.

[23] B.O. Dirr, B.K. Schmalhorst, Crack depth analysis of a rotating shaft by vibration measurement, *Journal of Vibration, Acoustics, Stress, and Reliability in Design—Transactions of the ASME* 110 (1988) 158–164.

[24] A.S. Sekhar, B.S. Prabhu, Vibration and stress fluctuation in cracked shaft, *Journal of Sound and Vibration* 169 (1994) 655–667.

[25] W.H. Beyer, *CRC Standard Mathematical Tables*, CRC Press, USA, 1979.

[26] O.S. Jun, J.O. Kim, Free bending vibration of a multi-step rotor, *Journal of Sound and Vibration* 224 (1999) 625–642.